Monthly Notices
of the
ROYAL ASTRONOMICAL SOCIETY

Mon. Not. R. Astron. Soc. **417,** 382–399 (2011) doi:10.1111/j.1365-2966.2011.19271.x

3D magnetohydrodynamic simulations of the evolution of magnetic fields in Fanaroff–Riley class II radio sources

M. Huarte-Espinosa,[1,2,3]★ M. Krause[4,5] and P. Alexander[2,3]

[1]*Department of Physics and Astronomy, University of Rochester, 600 Wilson Boulevard, Rochester, NY 14627-0171, USA*
[2]*Astrophysics Group, Cavendish Laboratory, 19 J. J. Thomson Avenue, Cambridge CB3 0HE*
[3]*Kavli Institute for Cosmology Cambridge, Madingley Road, Cambridge CB3 0HA*
[4]*Max-Planck-Institut für Extraterrestrische Physik, Giessenbachstrasse, 85748 Garching, Germany*
[5]*Universitätssternwarte München, Scheinerstr. 1, 81679 München, Germany*

Accepted 2011 June 15. Received 2011 June 14; in original form 2011 April 19

ABSTRACT

Radio observations of Fanaroff–Riley class II (FR II) sources often show correlations between the synchrotron emission and the linear-polarimetric distributions. Magnetic position vectors seem to align with the projected emission of both the radio jets and the sources' edges. Using statistics we study such relation as well as its unknown time evolution via synthetic polarization maps of model FR II sources formed in 3D magnetohydrodynamics numerical simulations of bipolar, hypersonic and weakly magnetized jets. The magnetic field is initially random with a Kolmogorov power spectrum, everywhere. We investigate the structure and evolution of magnetic fields in the sources as a function of the power of jets and the observational viewing angle. Our synthetic polarization maps agree with observations, showing *B*-field vectors which are predominantly aligned with the jet axis, and show that magnetic fields inside sources are shaped by the jets' backflow. Polarimetry is found to correlate with time, the viewing angle and the jet-to-ambient density contrast. The magnetic structure inside thin elongated sources is more uniform than inside more spherical ones. We see jets increase the magnetic energy in cocoons in proportion to the jet velocity and the cocoon width. Filaments in the synthetic emission maps suggest turbulence develops in evolved sources.

Key words: MHD – turbulence – methods: numerical – galaxies: active – intergalactic medium – galaxies: jets.

1 INTRODUCTION

Centimetric wavelength observations reveal synchrotron emission from extragalactic Fanaroff–Riley class II radio sources (FR IIs; Fanaroff & Riley 1974) and radio-loud quasars (see e.g. Bridle & Perley 1984, and references therein). Linear polarization fractions within ∼10–50 per cent are commonly seen in these objects. Polarization maps of these sources show patchy distributions which correlate with the luminosity distribution (see Saikia & Salter 1988, for a review). Projected magnetic field vectors are predominantly parallel to both the radio jets and the boundaries of radio lobes (Alexander, Brown & Scott 1984; Bridle & Perley 1984; Leahy, Pooley & Riley 1986; Black et al. 1992; Johnson, Leahy & Garrington 1995; Hardcastle et al. 1997, 1998; Leahy et al. 1997; Gilbert et al. 2004; Mullin, Hardcastle & Riley 2006). Strong emission gradients are often followed by the vectors perpendicularly, and when multiple hotspots are observed in one of the two radio lobes, the vectors seem to follow a line that would connect the hotspots. Linear polarization fractions of radio jets tend to be higher at the edges than at inner regions. Linear polarization fractions of radio lobes tend to be higher at the edges than at regions both inside and between the lobes (Saikia & Salter 1988).

The direction of the magnetic field component that is in the plane of the sky is often inferred by computing the Stokes parameters on the observed signal. It is possible to do the calculations inversely in order to model the polarimetry distribution that results from given magnetic field geometries (Laing 1981a; Jones 1988). Such studies indicate that magnetic fields in FR IIs seem to consist of a combination of ordered and disordered (anisotropic) fields along the jets and their vicinities, as well as a random component at the inner regions of radio lobes (Laing 1981b; Bridle & Perley 1984; Saikia & Salter 1988). Circumferential magnetic structures are also frequently observed in the outer edge of the sources (Bridle & Perley 1984; Saikia & Salter 1988).

Based on the radio luminosity distribution observed in several FR IIs, Rees (1971), Longair, Ryle & Scheuer (1973), Blandford & Rees (1974) and Scheuer (1974) proposed the following model for the plasma dynamics in the sources. Magnetized relativistic plasma jets are launched from a central engine located inside active galactic

★E-mail: martinhe@pas.rochester.edu

nuclei (AGN) which are typically seen at positions that match those of the radio cores. A cavity (the cocoon, hereafter) is inflated with the jets' plasma, and a strong bow shock is driven on the inter-cluster medium (ICM). Jets collide with the ambient medium at their working surfaces. Radio hotspots are seen at the leading edges of the lobes because the plasma pressure is the highest there. The plasma nearby is pushed towards the radio core and a backflow of magnetized plasma develops. Radio synchrotron lobes are thus formed, separated from the ICM by a contact discontinuity.

At kiloparsec scales, magnetic fields in FR IIs are often modelled in energy equipartition with the synchrotron emitting ultrarelativistic electrons. Magnetic flux freezing is expected to bond field lines and radio emitting electrons dynamically, hence the jets' backflow should play an important role in shaping magnetic fields inside cocoons (Laing 1980; Alexander et al. 1984; Leahy & Williams 1984; Miller 1985; Saikia & Salter 1988).

The expansion of radio sources must be considered to understand their inferred magnetic structure. Evolutionary models have provided analytical expressions for the global time dependence of the volume, the pressure and the energy inside cocoons (Scheuer 1974; Begelman & Cioffi 1989; Falle 1991; Kaiser & Alexander 1997; Heinz, Reynolds & Begelman 1998; Krause 2003). The large-scale features of the complex non-linear dynamics in such plasma cavities have been captured by numerical simulations (for reviews, see Norman 1993; Ferrari 1998; Pudritz et al. 2006). 2D axisymmetrical simulations of magnetized jets have confirmed the basic picture regarding jets (beams), lobes (cocoons) and bow shocks (e.g. Clarke, Norman & Burns 1986; Lind et al. 1989; Kössl, Müller & Hillebrandt 1990a,b; Frank et al. 1998; Komissarov 1999; Stone & Hardee 2000). These simulations also show that cocoons consist of a series of vortices. These structures arise in a complex feedback loop, where pressure modulations in the cocoons interact with the beams' shock pattern which, in turn, modifies the vortex shedding. The vortices decay in a turbulent cascade (cf. Section 3 in Krause & Alexander 2007). The latter process results in some degree of isotropization of the field lines which should affect the alignment of magnetic fields and the fractional polarization.

Further, the expansion of cocoons involves magnetic field amplification. This happens via two field line stretching processes (Matthews & Scheuer 1990b). The poloidal stretching mechanism, which arises because the fluid elements in the beam located close to the beam boundary take small turns, and thus end up towards the inner part of the cocoons. In contrast, the fluid elements close to the jet axis make larger turns and end up near the outer cocoon boundary. Because of the larger path-length of these fluid elements, they lag behind. Hence shear amplifies the magnetic field in cocoons along the direction of the jet axis. On the other hand, the toroidal stretching process amplifies the toroidal component of magnetic fields via cocoon expansion perpendicular to the jet axis. Unless the flow structure is axisymmetric, which is an unlikely configuration for real radio sources, the toroidal magnetic field may again be sheared, and thereby converted into poloidal field. To first order, the resulting magnetic field structure is determined by both, these competing processes and the initial condition. This picture has been refined by Gaibler, Krause & Camenzind (2009) who initialized their simulation with a helical magnetic field confined to the beam. The poloidal component of these fields returns to the source along, and close to, the beam, and therefore its strength drops steeply with distance from the jet axis, R. The radial cocoon expansion puts work into the toroidal field which, consequently, increases linearly with R, as predicted by Matthews & Scheuer (1990b, toroidal stretching). Hence, the magnetic energy in radio lobes could be largely due to dynamo action in the large-scale jet flow, with little dependence on the conditions (set-up) at the base of the beam. The literature on 3D jet simulations, in contrast, has not paid much attention to these issues. In general, one finds jet instabilities which are transparent to simulations with less degrees of freedom, e.g. jet fluting, deflection, disconnection and splash-back (see e.g. Norman 1993). Jet propagation has been studied also with relativistic magnetohydrodynamics (MHD) codes (e.g. Leismann et al. 2005; Keppens et al. 2008; Mignone et al. 2010, and references therein). These studies have not particularly focused on polarization properties. Relativistic jets have narrower cocoons for a given rest mass density ratio, and more stable beams. The motions in radio lobes are subrelativistic, and hence their physics should not be too much influenced by a relativistic nature of the jet.

Synthetic observations are produced using data from numerical simulations in order to compare them with observations. Matthews & Scheuer (1990a) simulated the hydrodynamic advection and polarized synchrotron emission of random, passive magnetic fields in AGN jets, finding high linear polarization fractions, of about 70 per cent. Clarke (1993) carried out 3D simulations of the interaction of a jet and a cloud with passive uniform magnetic fields. The synthetic synchrotron emission maps of Clarke showed filaments, formed by velocity shear. Hardee, Clarke & Rosen (1997) carried out 3D-MHD simulations of supermagnetosonic magnetized perturbed equilibrium beams, where a section of an infinitely long beam is studied, and found synthetic intensity structures similar to the ones observed in the jets of Cygnus A. More recently, Tregillis, Jones & Ryu (2004b) investigated the fractional polarization of synthetic synchrotron observations of 3D-MHD AGN jet simulations. They found rather high fractional polarizations in regions where shock acceleration increases the emissivity, but much smaller fractional polarization at regions where relativistic particles illuminate the volume more uniformly. In general, little attention has been given to the statistics of synthetic polarimetry and the way it relates with the properties of radio jets.

In this paper we present 3D-MHD numerical simulations of hypersonic magnetized jets as well as synthetic synchrotron and polarization observations. In contrast to Gaibler et al. (2009) and much other work, we do not start with a regular magnetic field component within the jet, but rely entirely on the field amplification due to the dynamics of cocoons (compare above) to create structure. Regarding analysis and the questions we address, we follow essentially Matthews & Scheuer (1990a) with the important improvement that here we use a full 3D-MHD treatment for the jet simulation.

This paper is organized as follows. In Section 2 we describe the formalism of ideal MHD and the numerical methods we use. Our implementations of the ICM, cluster magnetic fields (CMFs) and AGN jets are also described there along with details of our calculations for the synthetic synchrotron emission and polarimetry. In Section 3 we talk about the flow structure in our model sources and analyse it in terms of energetics. Synthetic maps are then presented and compared with FR II radio observations. The results are then interpreted and analysed statistically. Section 4 is dedicated to compare our models with previous numerical simulations. We then summarize and conclude our study in Section 5 which is followed by the bibliography.

2 SIMULATIONS

We describe the dynamics of plasma in the ICM and AGN radio jets using the system of non-linear time-dependent hyperbolic

Table 1. Simulations and parameters.

Simulation name	v_j [a] (Mach)	η [b]	L_j [c] ($\times 10^{38}$ W)	t_e [d] (Myr)
Lighter slow	40	0.004	4.6	14.1
Light slow	40	0.020	17.2	8.3
Lighter fast	80	0.004	28.1	7.1
Light fast	80	0.020	128.8	4.4
Lighter faster	130	0.004	112.8	4.7

[a] Time-averaged average jet velocity in the nozzle. It is equal to the external Mach number.
[b] Time-averaged average jet to ambient density contrast in the nozzle.
[c] Jet power from equation (11).
[d] Simulation end times.

equations of ideal compressible MHD. In three dimensions and non-dimensional conservative form, these are given by

$$\frac{\partial \rho}{\partial t} + \nabla \cdot (\rho \boldsymbol{V}) = \dot{\rho}_j \tag{1}$$

$$\frac{\partial (\rho \boldsymbol{V})}{\partial t} + \nabla \cdot (\rho \boldsymbol{V} V + p_g + B^2/2 - \boldsymbol{B}\boldsymbol{B}) = \rho \boldsymbol{g} + \dot{\boldsymbol{P}}_j \tag{2}$$

$$\frac{\partial E}{\partial t} + \nabla \cdot [(E + p_g + B^2/2)\boldsymbol{V} - \boldsymbol{B}(\boldsymbol{V} \cdot \boldsymbol{B})] = \dot{E}_j \tag{3}$$

$$\frac{\partial \boldsymbol{B}}{\partial t} - \nabla \times (\boldsymbol{V} \times \boldsymbol{B}) = 0, \tag{4}$$

where ρ, p_g, $\boldsymbol{V}$ and $\boldsymbol{B}$ are the plasma density, thermal pressure, flow velocity and magnetic fields, respectively. In equation (3), $E = p_g/(\gamma - 1) + \rho V^2/2 + B^2/2$ and represents the total energy density, whereas γ is the ratio of specific heats. In the right-hand side of equations (1), (2) and (3), source terms are used to implement jets by injecting mass, $\dot{\rho}_j$, momentum, $\dot{\boldsymbol{P}}_j$, and kinetic energy, $\dot{E}_j$ (see Section 2.2), as well as a Newtonian gravitational acceleration, $\boldsymbol{g}$, to keep the plasma in magnetohydrostatic equilibrium (see Section 2.1.1).

We solve the above equations in three dimensions using the numerical code FLASH 3.1 (Fryxell et al. 2000). FLASH's new multidimensional unsplit constrained transport solver is employed to maintain the divergence of magnetic fields down to $\lesssim 10^{-12}$ (Lee & Deane 2009). A diffusive HLLC solver (Batten et al. 1997) prevents spurious low pressure and density values from appearing in the grid. We use a Courant–Friedrichs–Lewy parameter of 0.25 and periodic boundary conditions in all the domain's faces. These boundary conditions prevent numerical noise from polluting the turbulent magnetic spectrum in the grid (Section 2.1.2). Our computational domain is a cube with edges $|\boldsymbol{x}| \leq 1/2$, in computational units, and has a uniform grid with 200^3 cells. This represents a volume of 200 kpc^3 meant to simulate the core of a cluster.

We carried out five jet simulations (see Table 1) designed to experiment with the power of jets in terms of their velocities and densities. Computations ran for approximately 12 h on 64 processors at the CamGrid[1] cluster of the University of Cambridge, and the production runs executed for about 4 h (using 64 processors) at the Darwin[2] supercomputer of the University of Cambridge High Performance Computing (HPC) facility.

2.1 Initial conditions

2.1.1 The ICM

The cluster plasma is implemented using an equation of state of an ideal monoatomic gas, with a ratio of specific heats $\gamma = 5/3$, a constant sound speed ($c_s^2 = \gamma p_g/\rho = 1$) throughout the domain and a density following a King profile (King 1972):

$$\rho_{\rm ICM}(r) = \frac{\rho_c}{[1 + (r/r_c)^2]^{3\beta/2}}, \tag{5}$$

where the central density, ρ_c, the central radius, r_c, and β take the values of 1, 0.8 and 2/3, respectively.

To keep the magnetized gas in magnetohydrostatic equilibrium, we implement a radial acceleration source term $\boldsymbol{g}$ to equation (2), and take the balance between this term and the total plasma pressure $p_g + B^2/2$. In the radial direction this term takes the form:

$$g_r = -\frac{2\,c_s^2}{\gamma r_c^2} \frac{r}{[1 + (r/r_c)^2]} \left(1 + \frac{1}{\beta_m}\right), \tag{6}$$

where β_m is the ratio of thermal pressure to magnetic pressure.

2.1.2 Cluster magnetic field

The magnetic field within the cluster is set up as an isotropic random field with a power-law energy spectrum. Following Tribble (1991b) and Murgia et al. (2004), we generate a cubic grid in Fourier space, with 200^3 cells. For each of these, we define three components of a vector potential which takes the form $\tilde{\boldsymbol{A}}(\boldsymbol{k}) = \boldsymbol{A}(\boldsymbol{k})e^{i\boldsymbol{\theta}(\boldsymbol{k})}$, where $\boldsymbol{k}$ is the frequency vector ($k^2 = k_x^2 + k_y^2 + k_z^2$), 'i' is the unitary complex number, while $\boldsymbol{A}$ and $\boldsymbol{\theta}$ are the vector amplitudes and phases, respectively. We draw $\boldsymbol{\theta}(\boldsymbol{k})$ from a uniform random distribution within 0 and 2π, and $\boldsymbol{A}(\boldsymbol{k})$ is also randomly distributed but has a Rayleigh probability distribution

$$P(A, \theta)\,{\rm d}A{\rm d}\theta = \frac{A}{2\pi |A_k|^2} \exp\left(-\frac{A^2}{2|A_k|^2}\right) {\rm d}A{\rm d}\theta, \tag{7}$$

where we choose the power law ansatz

$$|A_k|^2 \propto k^{-\zeta}, \tag{8}$$

for a given slope ζ.

We transform to real space by taking the inverse fast Fourier Transform (Press et al. 1992) of $\tilde{\boldsymbol{A}}(\boldsymbol{k})$. The resulting magnetic vector potential, $\boldsymbol{A}(\boldsymbol{x})$, is multiplied by the plasma density radial profile (5). This product implements magnetic flux freezing by generating fields, the strength of which follows the plasma density, and pressure, profile. The components of the vector potential are then read and mapped into the staggered-grid cell interfaces of FLASH 3.1, and the curl of this vector is then calculated to give the magnetic field. Finally, we normalize the resulting field so that the ICM's thermal pressure is approximately 10 times larger than its magnetic pressure [$\beta_m = p_g/(B^2/2) \sim 10$] everywhere in the grid, which is a reasonable value in this context (Carilli & Taylor 2002).

This procedure yields solenoidal magnetic fields tangled at scales of order our computational resolution and characterized by spatial

[1] http://www.escience.cam.ac.uk/projects/camgrid/

[2] http://www.hpc.cam.ac.uk/darwin.html

variations following a magnetic power spectrum with a power law of the form:

$$|B|^2 \propto k^{-\zeta+2} = k^{-n}, \tag{9}$$

where we choose a Kolmogorov 3D turbulent slope $n = -11/3$, based on the work of Vogt & Enßlin (2003, 2005) and Guidetti et al. (2008). We use the same realization for all our runs. We note that the Fourier method implicitly imposes maximum and minimum scale on the field.

We let this plasma relax for one crossing time before injecting the jets.

2.2 Jets

By implementing source terms to equations (1), (2) and (3), we inject mass, x-momentum and kinetic energy to the central grid cells that are within a control cylinder of radius r_j and height h_j, resolved by three and eight cells, respectively. Inside this 'nozzle' we update the plasma density and x-velocity via constant source terms $\dot{\rho}_j$ and $\dot{v}_j$. Jets are continuously injected until they reach the computational boundaries and then the simulations are stopped. Plasma pressure in the nozzle, p_j, takes the constant value of the central ambient pressure (i.e. ρ_c/γ). The jet density is computed using $\rho_j = \eta\rho_c$, where the parameter η takes the (low) values given in Table 1. We assume an ideal gas equation of state with $\gamma = 5/3$ for the jet material. The light densities of our jets are motivated by the work of Alexander & Pooley (1996) and Krause (2003), and their high Mach numbers are based on the observed jets sidedness associated with Doppler beaming, suggesting that FR II sources are at least close to relativistic up to scales of order 100 kpc (Mullin & Hardcastle 2009). The Mach numbers of our jets with respect to the sound speed in the ambient gas are 40, 80 and 130, which correspond to velocities close to 66 $\times 10^3$, 133 $\times 10^3$ and 216 $\times 10^3$ km s^{-1}, respectively. The Mach numbers of the jets with respect to the sound speed in the beam material are 2.5, 5.7, 5, 11.3 and 8.2, as they appear in Table 1. We extend the implementation of Omma et al. (2004) to simulate bipolar magnetized jets. The launch and collimation of the jets are assumed to occur in the AGN 'central engine' located at sub-resolution scales.

The initial jet magnetic fields are kept from the initialization of the ambient medium, and no magnetic source term is applied. It therefore has a random topology, an average $\beta_m \sim 10$ and, given the assumed power spectrum (Section 2.1.2), it is fairly uniform at scales $\sim r_j$. We note, however, there is no reason to believe the magnetic fields in FR II radio jets are related to the CMFs near the AGN; jet fields are expected to be advected up the beam from the central engine. Our choice of initial jet magnetic fields is based on the fact they seem to be weak at kiloparsec scales and to have a random component (Section 1). This is the case of the central fields in our model.

As our jets propagate, their magnetic fields are deformed by shear. The time-averaged average beam β_m is of about 50. The power of jets is the sum of thermal and kinetic power terms:

$$L_j = \int \left(\frac{1}{2}(\eta\rho_c)v_j^2\right) v_x \, dA + \int \left(\frac{\gamma p_j}{\gamma - 1}\right) v_x \, dA, \tag{10}$$

which takes the following form at the grid:

$$L_j = \frac{1}{2}\left(\eta\rho_c\right)(\pi r_j^2)v_j^3 + \frac{\gamma}{\gamma - 1} p_j \left(\pi r_j^2\right) v_j. \tag{11}$$

2.2.1 *Cocoon contact surface*

We use a passive incompressible tracer, $\tau(\boldsymbol{x}, t)$, which is injected with the jet plasma to distinguish it from that of the ambient medium. When jet injection starts, $\tau(\boldsymbol{x}, t_{jet} = 0)$ takes the values of 0.99 and 1×10^{-10} at the nozzle and at the ICM, respectively. The tracer is then advected with the jet gas and takes values within 1×10^{-10} to 0.99. A comparison of the distributions of τ and ρ allows us to identify the contact surface of the cocoon with an accuracy up to four computational cells.

2.3 Synthetic radio maps

Our simulations produce 3D data cubes with information about the distribution of the magnetized gas in our model sources at different times during their expansion. Synthetic synchrotron emission and polarimetry are computed under the assumption that the radiation is linearly polarized. Beaming and light-travel effects are assumed to be negligible. Synthetic observations are produced at viewing angles, θ_v, of 30°, 60° and 90° measured from the jet axis to the line of sight (thus jets are in the plane of the sky when $\theta_v = 90°$). Given a viewing angle and a simulation time-step, t, Stokes parameters are (i) calculated for every computational cell inside the source, using the magnetic field components in the plane of the sky, $\boldsymbol{B}'(\boldsymbol{x}, t)$, (ii) integrated through the source, along the line of sight, $Z_\parallel(t)$. Mathematically,

$$\begin{aligned}
I(\boldsymbol{x}_\perp, t) &= \frac{1}{l}\int_0^l \delta(\tau)\,\tau(\boldsymbol{x}, t)\, p_c(\boldsymbol{x}, t)\,[B'_x(\boldsymbol{x}, t)^2 \\
&\qquad + B'_y(\boldsymbol{x}, t)^2]\, dZ_\parallel(t), \\
Q(\boldsymbol{x}_\perp, t) &= \frac{0.75}{l}\int_0^l \delta(\tau)\,\tau(\boldsymbol{x}, t)\, p_c(\boldsymbol{x}, t)\,[B'_x(\boldsymbol{x}, t)^2 \\
&\qquad - B'_y(\boldsymbol{x}, t)^2]\, dZ_\parallel(t), \\
U(\boldsymbol{x}_\perp, t) &= \frac{0.75}{l}\int_0^l \delta(\tau)\,\tau(\boldsymbol{x}, t)\, p_c(\boldsymbol{x}, t)\, 2\, B'_x(\boldsymbol{x}, t) \\
&\qquad B'_y(\boldsymbol{x}, t)\, dZ_\parallel(t),
\end{aligned} \tag{12}$$

where

$$\delta(\tau) = \begin{cases} 1 & \text{for } \tau(\boldsymbol{x}, t) \in [0.5, 0.99] \text{ (cocoon)}; \\ 0 & \text{for } \tau(\boldsymbol{x}, t) \in [1 \times 10^{-10}, 0.5) \quad \text{(ambient)}, \end{cases} \tag{13}$$

and $\boldsymbol{x}_\perp$, $p_c(\boldsymbol{x}, t)$ and I represent the coordinates in the plane of the sky, the distribution of the cocoon pressure and the total intensity of the radiation, respectively. We note equation (12) are valid for a synchrotron emission spectral index $\alpha = 1$, yet the degree of polarization we predict does not vary too much with α (Laing 1980). The factor of 0.75 in the expression of Q and U in (12) accounts for the maximum degree of linear polarization for a uniform magnetic field and a power-law electron energy distribution. We model the density distribution of synchrotron emitting electrons via the factor $\tau(\boldsymbol{x}, t)\, p_c(\boldsymbol{x}, t)$ in (12). We do not follow any explicit energy gain or loss processes such as synchrotron cooling or shock acceleration (i.e. the background plasma pressure is proportional to the constant factor in the energy distribution of relativistic electrons). A detailed treatment of the electron distribution is beyond the scope of this paper. We note that we have also tried a constant density of radiating electrons, which did not significantly change the results. The polarization angle of the magnetic vectors, χ_B, and the degree of

linear polarization (= fractional polarization), p, are given by

$$\chi_B = \frac{1}{2}\arctan(U/Q) + \frac{\pi}{2}, \qquad p = \frac{\sqrt{U^2+Q^2}}{I}. \tag{14}$$

3 RESULTS AND ANALYSIS

Synthetic polarization and emission maps are presented in pairs characterized by the jet velocity (same as the external Mach number), the density contrast, η, the viewing angle, θ_v, and the time that jets have been active, t_{jet}. Polarization maps have a constant vector density of 0.5 cells^{-2}.

3.1 Flow structure

The hydrodynamic flow structure of our simulations is very similar to what is generally found in the literature (cf. Section 1, above, Fig. 1). The hypersonic jets flow straight for a certain distance (2D-phase). Then 3D instabilities develop, more clearly in the lighter jet runs, and the jet head oscillates around the jet axis, consistently with Scheuer's dentist drill (3D-phase). Cocoons are wider for lower jet density and faster jets, as expected. The relatively heavier jets ($\eta = 2 \times 10^{-2}$) propagate faster in the axial direction, and backflows in their cocoons are much less turbulent than in their relatively lighter ($\eta = 4 \times 10^{-3}$) counterparts.

The evolution of cocoon magnetic fields is driven by the following dynamics. The field is initially random inside the jet injection volume. The injected momentum stretches field lines along the jet direction. This puts energy into the axial field, which is therefore amplified. The other field components are simply advected out of the injection volume, and their field strength drops with time, within the injection volume and the beam. This process results in a poloidally dominated magnetic field, similar to the setup in Gaibler et al. (2009), yet with some important differences. First, the field in the axial direction is patchy (cf. Fig. 2 for this and other details of the magnetic field), i.e. adjacent parts of the beam have the field parallel and antiparallel to the flow direction. Secondly, for a given plane perpendicular to the flow vector, the field may in principle also be patchy, i.e. there is not necessarily one dominant toroidal field loop, but possibly two or more field loops across a section of the jet. However, the fact that the power spectrum used for the initial field setup strongly favours larger scales, still produces a predominantly toroidal configuration for the magnetic field perpendicular to the jet axis.

As Gaibler et al. (2009) do, we find that the axial field lines return to the injection region very close to the jet. In our case, this may even happen inside the beam, since any beam cross-section may in general contain axial field patches of opposing directions. In the presence of a backflow, this requires field line reconnection, which should be easily possible in the jet head on numerical grounds due the complex flow pattern in this region. This seems to suggest that the general structure of the poloidal magnetic field does at least not very much depend on the initial conditions. The reason is that the elongation of the beam stretches the axial field lines and therefore amplifies the axial field. To have the field lines going out in the beam and returning close to it or even within is the configuration which requires the least amount of energy, and is therefore chosen by the system.

Gaibler et al. (2009) find the toroidal part of the field, which cannot be lost to other field components via turbulence due to the axisymmetry condition in their study, increases linearly with distance from the jet axis. This may be easily understood from the induction equation. The physical reason is the work done by the expanding cocoon on the toroidal field component is stored in that part of the magnetic field. We do not observe such a linear increase in the toroidal field in our 3D simulations directly, but we expect this process also to be at work. Since it is related to the cocoon expansion, we expect more magnetic energy to be created by fatter cocoons, i.e. for lower jet density (most important for the cocoon width), and higher jet velocity, which is also found by Gaibler et al. (2009). They also show that this process is able to enhance the total magnetic energy in the jet by a factor of a few (see their fig. 20). For our simulations, therefore, we expect a noticeable increase in the magnetic energy during the simulation time; the fatter the cocoons the higher the energy rise. Fig. 3 shows this expectation is exactly what we find. Here we plot the magnetic energy in both the cocoon and beam over the source size for all runs. The curves are indeed strictly ordered according to cocoon width. All the lighter jets have more magnetic energy than any of the light ones. Among jets with a given density, the faster ones have more magnetic energy. Therefore, the underlying reason for the increase of the magnetic energy is the increase of the toroidal component due to the cocoon expansion, just as in Gaibler et al. (2009). There is another detail that confirms this finding: as described above, we find the usual 2D- and 3D-phases for our jet simulations. The described amplification mechanism is very different in each phase. During the 2D-phase, field loops released in the jet head expand axisymmetrically, and substantial work is required to stretch the m. Energy from this work is later found in the magnetic field. In contrast, during the 3D-phase the dentist's drill moves the jet head away from the axis in different directions. Field loops therefore do not have to expand to reach large distances from the axis. They may keep their size and get pushed into different corners of the cocoon at different times. Hence, once cocoon inflation reaches and goes throughout the 3D-phase, almost no work is put into the field anymore. We believe this mechanism causes the turnover in the magnetic energy seen in Fig. 3. This turnover is visible for all the lighter jets at the comparable source size. The light jets, on the other hand, do not show much of an amplification in the first place, and also remain quite straight, i.e. essentially in the 2D-phase up to the end of the simulations. As expected, we do not find the turnover there. We note that a similar turnover is not found in the axisymmetric simulations by Gaibler et al. (2009) either, which is of course expected if it is linked to the 3D-phase.

Why do we not see a linear increase with distance from the jet axis in the toroidal field like Gaibler et al. (2009)? Because of the 3D nature of the cocoon turbulence in our simulations. While axisymmetric turbulence can only stretch and compress a given toroidal field, 3D turbulence may also turn toroidal field into poloidal one. The result is a turbulent cocoon field, with no geometrical similarity to the 2D result.

We see a strong axial field along the edge of the cocoons (see Fig. 2). This is due to velocity shear in this region (Section 4) where the time-averaged average backflow speeds with respect to the ambient medium are about 5×10^3, 5×10^3, 28×10^3, 22×10^3 and 27×10^3 km s^{-1}, for the sources as they appear in Table 1.

In the shocked ambient gas, on the other hand, magnetic fields are first compressed in the bow shock, and then reduced again due to adiabatic expansion of the gas, as it leaves the shock towards the cocoon. The effects of cocoon expansion on CMFs will be investigated in a sequel paper (Huarte-Espinosa, Krause & Alexander, in preparation).

The flow structure in our simulated radio sources is dominated by large-scale motions, namely the toroidal and poloidal stretching mechanisms we have discussed in this paper. We

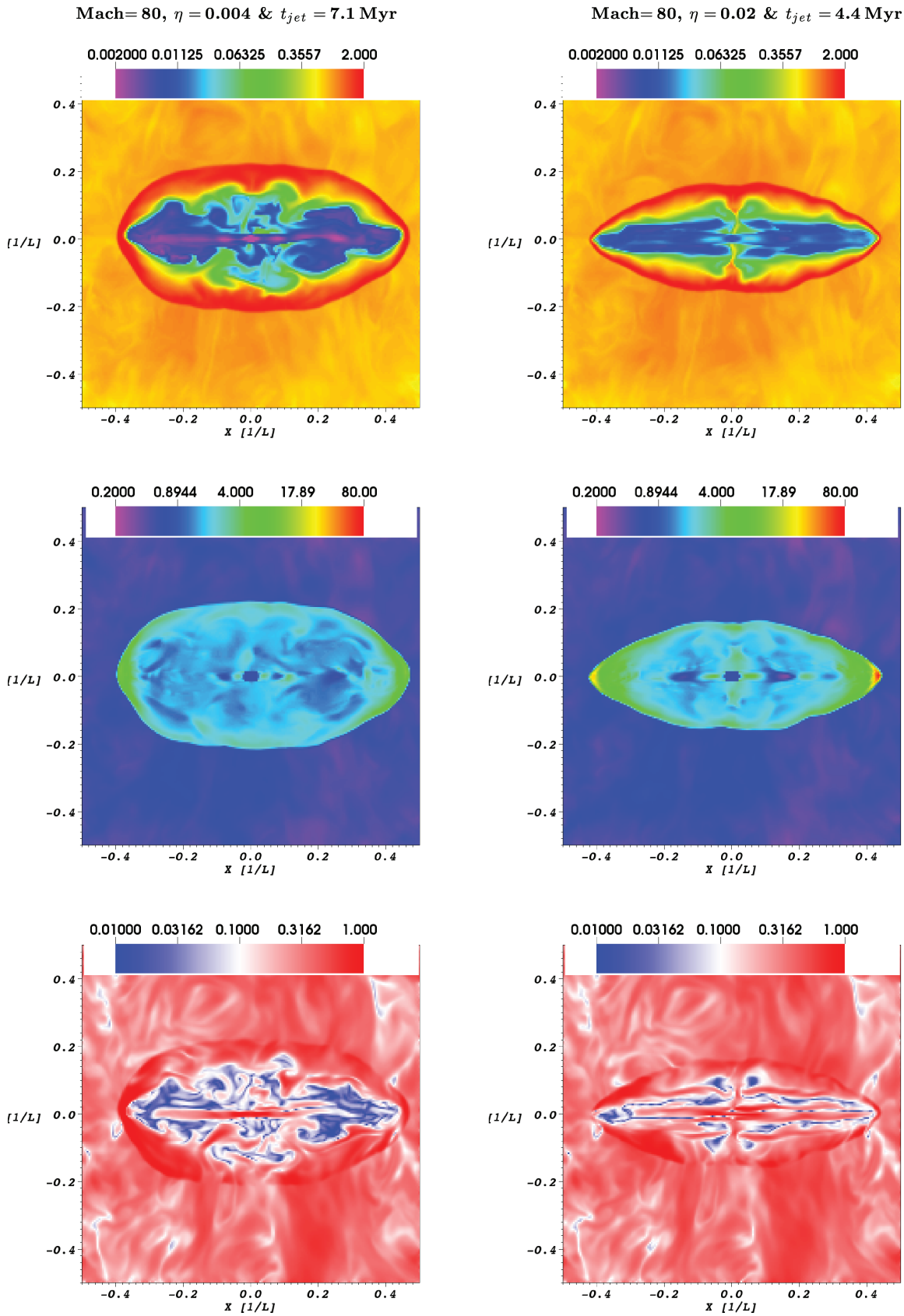

Figure 1. 2D cuts ($z = 0$) of the density (top row), the pressure (middle row) and the magnetic field strength (bottom row) distributions. The Mach number and density of the runs are given on the top of each column. Colour scales are logarithmic and show variables in corresponding computational units. We see a clear relation between the intrinsic structure of sources and the resultant field structure in the synthetic polarization maps (Figs 4–8).

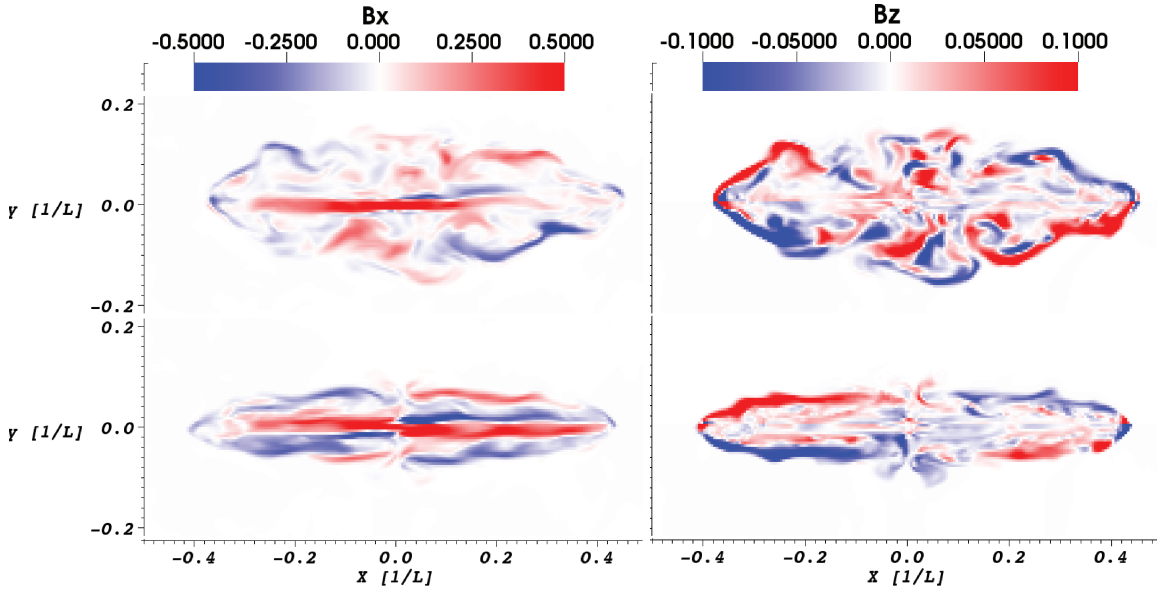

(a) Axial magnetic field (left) and toroidal magnetic field (right). $\eta = 0.004$ (top) and $\eta = 0.02$ (bottom).

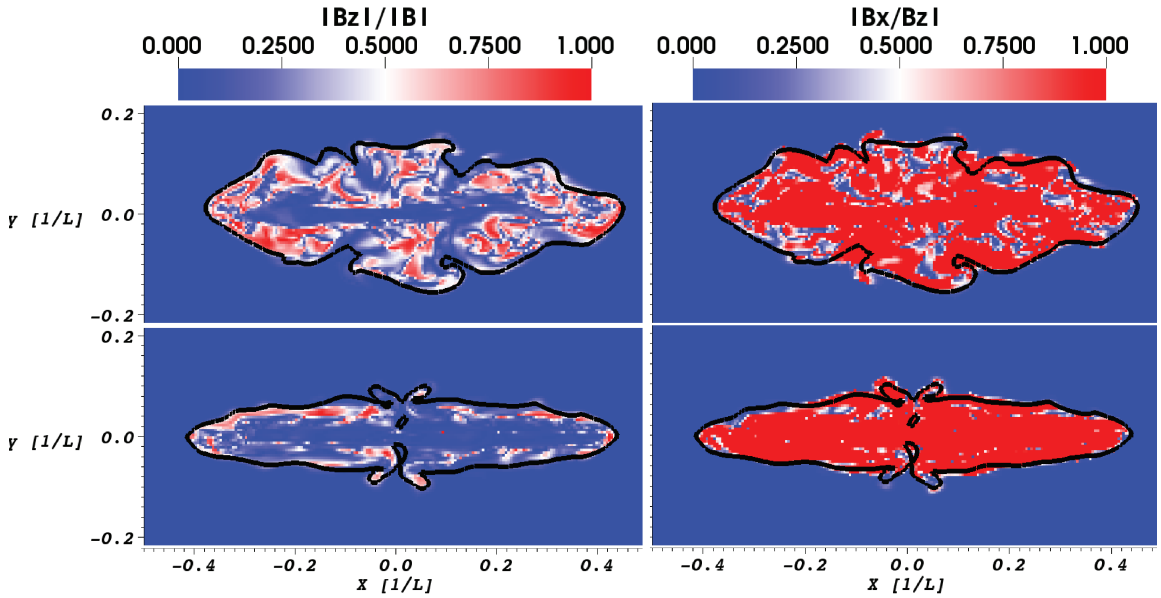

(b) Toroidal over total magnetic field (left) and axial over toroidal magnetic field (right). $\eta = 0.004$ (top) and $\eta = 0.02$ (bottom). The cocoon contact surface is marked with a thick black line.

Figure 2. 2D cuts ($z = 0$) of the magnetic fields for the Mach 80 jets (see Table 1). Colour scales are linear and show variables in corresponding computational units.

cannot claim to represent the turbulence in our simulated cocoons well, because the resolution is too poor. Higher resolution should add additional small-scale structure, unless prevented by a sufficiently strong magnetic field (cf. e.g. Krause & Camenzind 2001). Yet, also turbulence is expected to have most power on large scales. Therefore, while higher resolution studies will still be useful, we would expect the results discussed in this paper to hold.

3.2 Synthetic radio maps

In Figs 4, 6, 7 and 8, we present synthetic radio and polarization angle maps of four of our simulated FR II radio sources (all but the lighter relativistic one) for three different snapshot times. These maps essentially reflect the field structure discussed above. The emission is dominated by filaments, hotspots and sometimes jets are seen. This is similar to what has been found in earlier studies, as detailed in the Section 1. The jet head region is more prominent at earlier times and for higher jet density. Our lighter jets feature more diffuse jet heads reminiscent of the *shock web complex*, described by Tregillis, Jones & Ryu (2001). Our polarization angle maps are all dominated by larger patches. This is due to the fact that the cocoon dynamics is dominated by large vortices, about the cocoon radius in diameter. The backflow in our $\eta = 0.02$ jets remains quite smooth and, consequently, the polarization vectors are even more parallel to the jet axis than they are in the lighter η sources. Generally, we

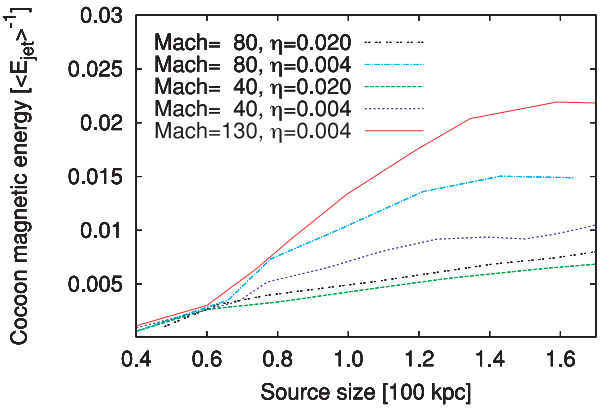

Figure 3. Time evolution of the magnetic energy in the cocoon. Only the $\eta = 0.004$ sources show flat gradients, typical of MHD turbulent dynamos.

find an almost one-to-one correspondence between the flow field and the polarization vectors, as expected.

In addition, in panel (b) of Figs 4, 6, 7 and 8 we show synthetic radio and polarization angle maps at different viewing angles. We consistently see that at small angles the axial field component gets smaller due to the projection effect, while other field components become relatively more prominent.

The patchy distributions in our polarization maps are in good agreement with typical observations of FR II sources and radio-loud quasars (see e.g. Bridle & Perley 1984; Saikia & Salter 1988; Gilbert et al. 2004; Mullin et al. 2006). Along the projected direction of jets, we see that $|\chi_B| < 20^\circ$, which are smaller angles than elsewhere inside the cocoon. For $\eta = 0.02$, $|\chi_B|$ increases progressively along the vertical direction, from the jet axis to the edge of sources (Figs 7 and 8). This is because in these simulations cocoons are narrow, and therefore the beam contributes significantly to the emission, which is not the case in most of the observed sources. In contrast, for $\eta = 0.004$, $|\chi_B|$ shows weak trends along the vertical direction. The outermost vectors in all the maps are commonly tangent to the dimmest emission contours. This is similar to observations, but is of course influenced by numerical problems at the contact surface, as outlined above.

Polarization degrees within 37–51 per cent are found inside cocoons, but higher, up to ~ 63 per cent, both at the edge of sources and at the position of jets. We often see uniform patches with very similar values of $|\chi_B|$ and p at the position of bright emission shocks. The vectors frequently follow strong intensity gradients perpendicularly and have p $\gtrsim$50 per cent. Regions of non-uniform $|\chi_B|$, on the other hand, are frequently located between emission shocks (see e.g. Fig. 4). These correlations are in good agreement with observations (e.g. see Högbom 1979; Laing 1981a; Bridle & Perley 1984; Saikia & Salter 1988; Hardcastle et al. 1997; Leahy et al. 1997; Gilbert et al. 2004) and with models of plasma compression and shear (e.g. Laing 1981b; Miller 1985).

Our synthetic emission maps often show hotspots at the location of the jets' working surfaces as well as filaments in the radio lobes. Radio hotspots and filaments are often seen in well-resolved FR II sources (e.g. Cygnus A, Perley, Dreher & Cowan 1984).

We see the backflows of the (antiparallel) jets collide and form sheets near the cocoon equatorial plane (the one normal to the jets and containing the central engine). There, our polarization maps show B-vectors with $|\chi_B| > \pi/4$ above and below the centre of Figs 4–8 (left column). We found instances of such polarization angle distributions in the observations of 3C 34, 3C 336 and 3C 341 (Johnson et al. 1995, Mullin et al. 2006 and Gilbert et al. 2004, respectively).

At the end of the simulations, we see laminar flows in the cocoons and also that both Rayleigh–Taylor and Kelvin–Helmholtz instabilities are growing at the contact surface (Fig. 1). Such flows form tube-like structures or filaments, as we see in our synthetic emission maps (Figs 4–8). Fig. 9 shows emission maps of the right lobe of the model source with $\eta = 0.004$, Mach $= 40$ and $t_{\rm jet} = 14.1$ Myr, for viewing angles of 30°, 60° and 90°. It is clear that the structure at the centre of the figures gets shorter and dimmer as the viewing angle decreases. This suggests a tube-like geometry for this feature. All our synthetic emission maps show filaments; however, we note that they form earlier in the low-η sources than in the high-η ones.

3.3 Polarimetry and statistics

In order to analyse our synthetic observations, we have produced histograms of the polarization angle and the degree of linear polarization; see Figs 10 and 11, respectively. In what follows, we will see that these distributions show a clear correlation with the viewing angle, the jet-to-ambient density contrast and time too, but only a weak dependence on the jet velocity.

3.3.1 The role of the viewing angle

The polarization angle histograms are similar for all runs at $\theta_{\rm v} = 90^\circ$. They are all peaked towards 0°, corresponding to the jet direction. The more isotropic distribution at lower viewing angle is consistent with cocoon turbulence. We see only the distribution of the heavier jets remains peaked at a viewing angle of 60°, because of the weaker cocoon turbulence in these sources, relative to the ones with lighter jets. This confirms the magnetic field structure is determined by the relative importance of turbulence as well as the amplification of the axial field due to the backflow in cocoons.

For $\theta_{\rm v} = 30^\circ$, 60° and 90°, the mean value of $|\chi_B(\eta = 0.004)|$ is generally larger than that of $|\chi_B(\eta = 0.02)|$ (see Section 3.3.2, below). The dispersion of the polarization angle seems to follow this trend as well. The differences are pronounced for viewing angles of 60° and 90°, and related to the size of the data sample, i.e. the cocoons' volume, which is inversely proportional to η in a non-linear way (Section 3.1). Polarization angle histograms at $\theta_{\rm v} = 30^\circ$ show both the flattest gradients and the least number of vectors amongst all histograms, and their distribution does not show a Gaussian functional form.

As the viewing angle increases we find the mean polarization angle, $\langle|\chi_B|\rangle$, decreases non-linearly (see Fig. 10; panel b, Figs 4–8). On average, $|\chi_B|$ diminishes for about 9° for viewing angles from 30° to 60°, and about 4° for viewing angles from 60° to 90°. Cocoons have geometries that resemble prolate spheroids, and thus magnetic fields inside them should relax easier along the jet axis than towards the equator. However, to produce the synthetic maps we follow two steps: (i) rotate the sources anticlockwise, perpendicularly to the jets and (ii) project them on to the plane of the sky. Hence only the magnetic component along the jet axis (the horizontal one in the maps) is affected in this process and grows in proportion to $\cos(\theta_{\rm v})$.

The dependence of the degree of linear polarization on the viewing angle is relatively modest and particularly evident for $\eta = 0.02$ (Fig. 11). We see $\langle p\rangle$ increases about 7 per cent from $\theta_{\rm v} = 30^\circ$ to 60°, and also about ~ 3 per cent from $\theta_{\rm v} = 60^\circ$ to 90°. Hereafter, $\langle p\rangle$ represents the arithmetic mean of p. For all η, the number of pixels in the polarization degree histograms consistently scales up with the viewing angle, in relation to the projected area of cocoons.

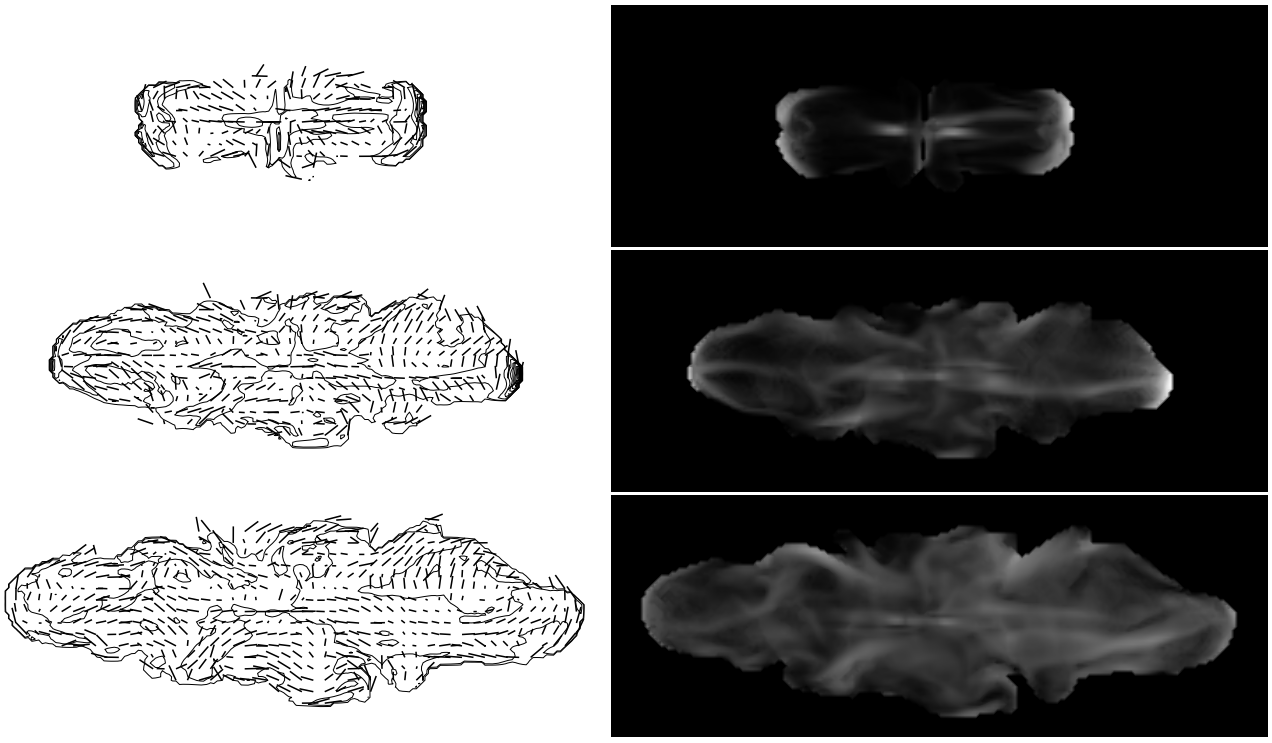

(a) Time evolution at $\theta_{\rm v} = 90°$. From top to bottom $t_{\rm jet} = \{4.7, 9.5, 14.1\}$ Myr.

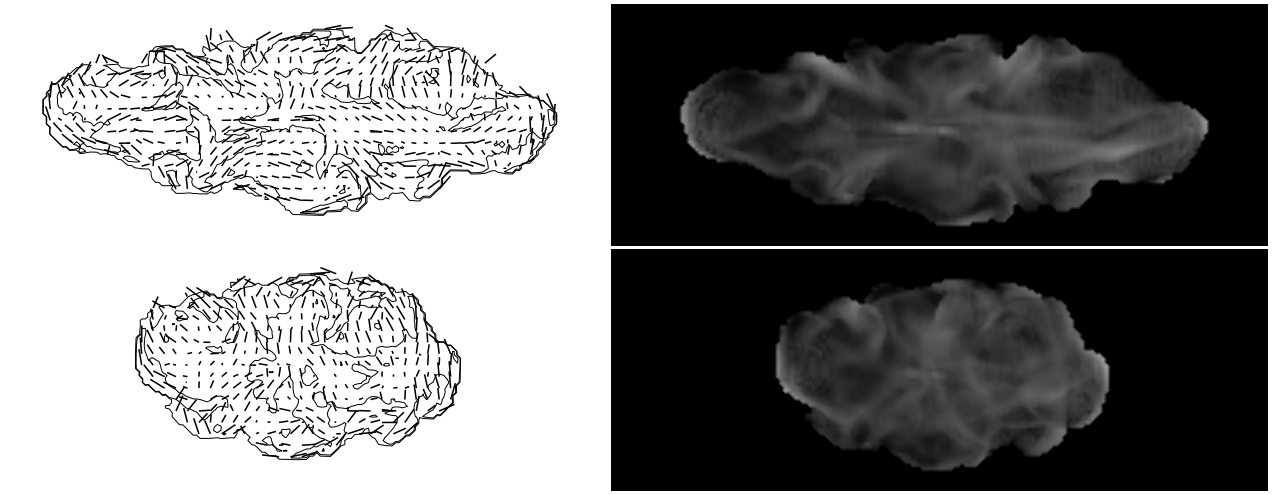

(b) Emission at $t_{\rm jet} = 14.1$ Myr as a function of the viewing angle; $\theta_{\rm v} = 60°$ (top) and $\theta_{\rm v} = 30°$ (bottom).

Figure 4. Synthetic observations of the source with $\eta = 0.004$ and Mach = 40. Left: polarization maps. Vectors follow χ_B and their length is given by p. Vectors are superimposed on linear contours of $I/\langle I\rangle$. Right: logarithmic grey-scale maps of $I/\langle I\rangle$.

3.3.2 The role of the density contrast

The jet-to-ambient density contrast is well known to be important for the evolution of cavities formed by astrophysical jets (see e.g. Krause 2003). Our synthetic maps show the density contrast also plays an important role on the radio source polarimetry. In general, the projected area of sources is inversely proportional to η in a non-linear way. Thus we see less magnetic fields in polarization measurements with $\eta = 0.02$ than with $\eta = 0.004$.

Given a time-step and a viewing angle, we find the mean polarization angle is typically $\sim 10°$ smaller for $\eta = 0.02$ than for $\eta = 0.004$. We see the spatial distribution of the polarization angle is more uniform for $\eta = 0.02$ than for the lighter case. For example, gradients greater than about $10°$ per computational cell ($10°$ kpc^{-1})

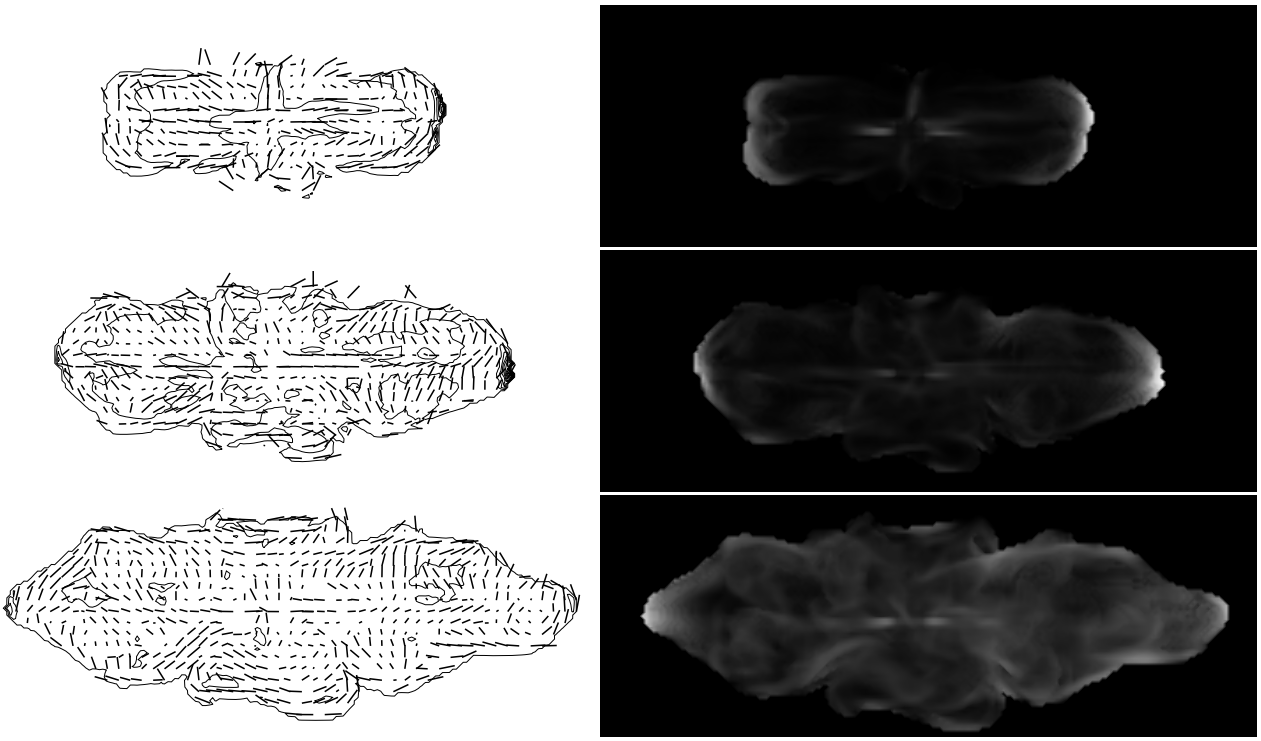

(a) Time evolution at $\theta_v = 90°$. From top to bottom $t_{jet} = \{3.6, 5.3, 7.1\}$ Myr.

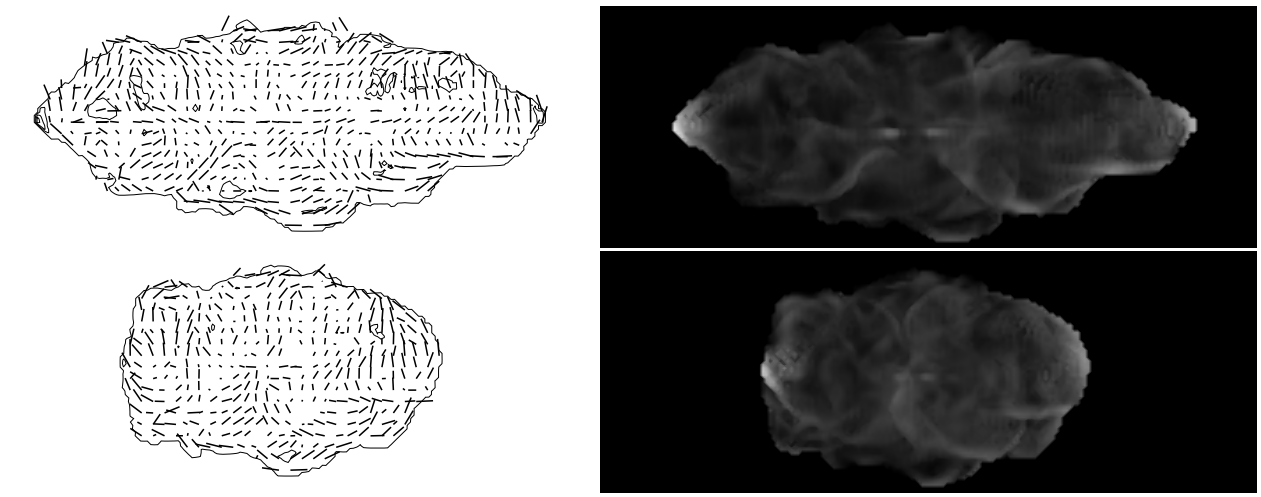

(b) Emission at $t_{jet} = 7.1$ Myr as a function of the viewing angle; $\theta_v = 60°$ (top) and $\theta_v = 30°$ (bottom).

Figure 5. Synthetic observations of the source with $\eta = 0.004$ and Mach = 80. Left: polarization maps. Vectors follow χ_B and their length is given by p. Vectors are superimposed on linear contours of $I/\langle I\rangle$. Right: logarithmic grey-scale maps of $I/\langle I\rangle$.

are less frequent in Fig. 4 (left column) than in Fig. 7, corresponding to $\eta = 0.02$ and 0.004, respectively.

The statistical behaviour of the polarization degree is very different. Given a time-step and a viewing angle, we frequently find higher values of the mean polarization degree for $\eta = 0.02$ than for the lighter case. On average, $\langle p\rangle(\eta = 0.02) \sim 47$ per cent, while $\langle p\rangle(\eta = 0.004) \sim 42$ per cent. Moreover, the polarization degree histograms follow Gaussian-like distributions. The mean polarization degree at large viewing angles increases with time for the heavier jets, indicating that axial field line stretching gets even more important with time. Conversely, it decreases with time for the lighter jets, which shows that turbulence gets even more important with time for the lighter jets. The polarization degree of the lighter jets does not depend on the viewing angle.

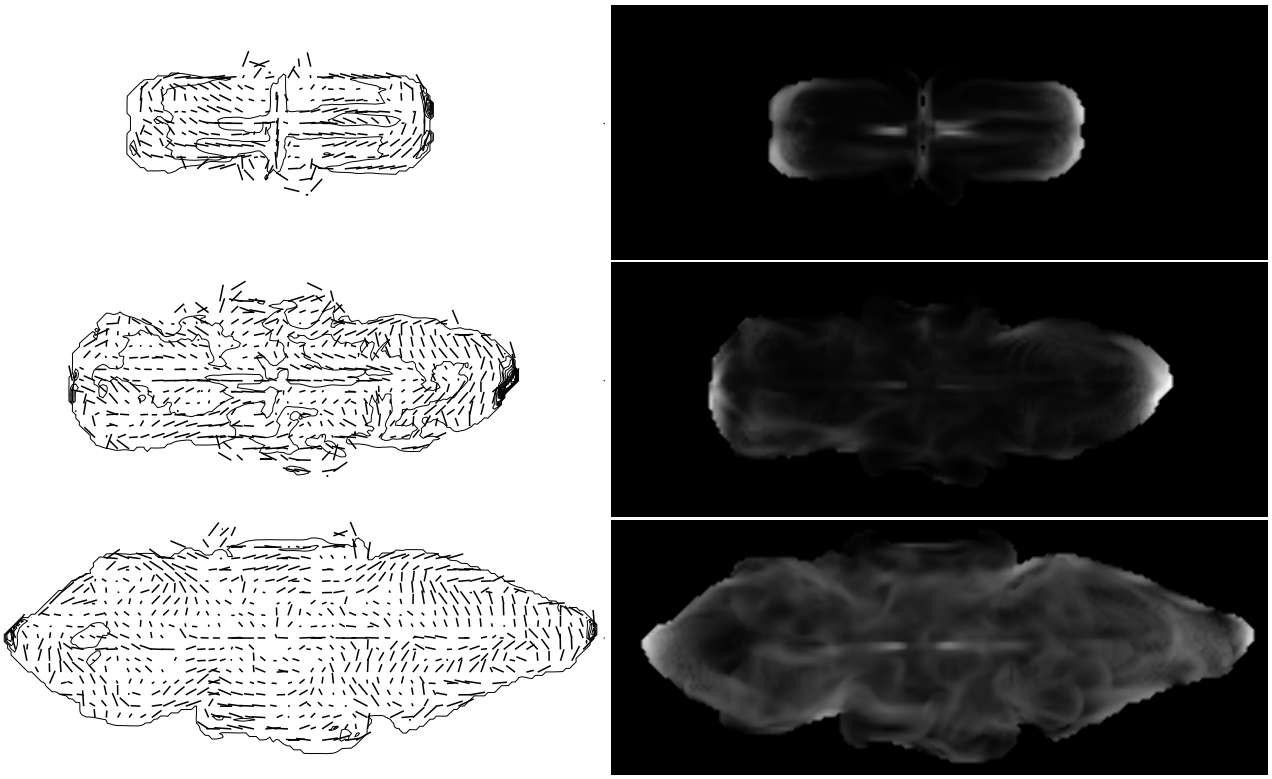

(a) Time evolution at $\theta_{\rm v} = 90°$. From top to bottom $t_{\rm jet} = \{1.9, 3.3, 4.7\}$ Myr.

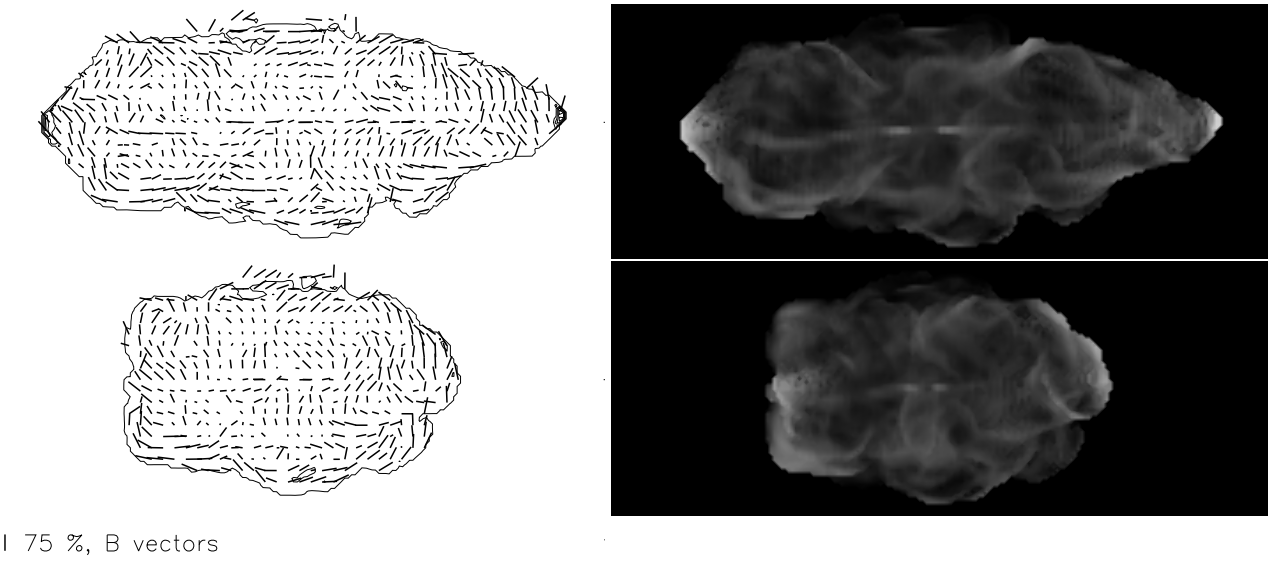

(b) Emission at $t_{\rm jet} = 4.7$ Myr as a function of the viewing angle; $\theta_{\rm v} = 60°$ (top) and $\theta_{\rm v} = 30°$ (bottom).

Figure 6. Synthetic observations of the source with $\eta = 0.004$ and Mach = 130. Left: polarization maps. Vectors follow χ_B and their length is given by p. Vectors are superimposed on linear contours of $I/\langle I\rangle$. Right: logarithmic grey-scale maps of $I/\langle I\rangle$.

3.3.3 Polarimetry evolution

The main features of the polarization angle histograms seem to be shaped during the early expansion phase of the model sources, particularly for viewing angles of 60° and 90°. Here, magnetic fields tend to align with the jet axis ($\chi_B = 0°$) as sources expand (panel *a*, Figs 4–8). The considered histograms decline steeply up to about 20°–40°, and remain roughly constant for higher χ_B. The constant part is at a very similar level for all viewing angles of a given simulation. These findings correspond to the effects of

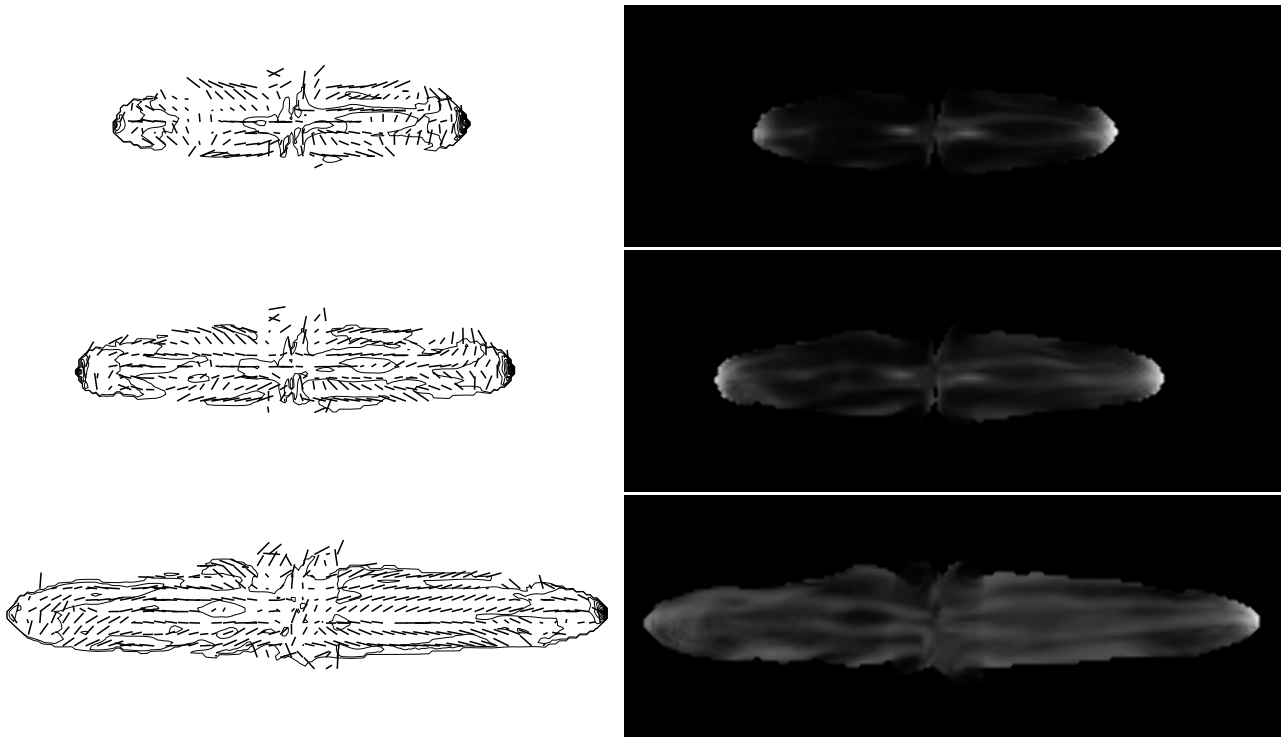

(a) Time evolution at $\theta_v = 90°$. From top to bottom $t_{jet} = \{4.7, 5.9, 8.3\}$ Myr.

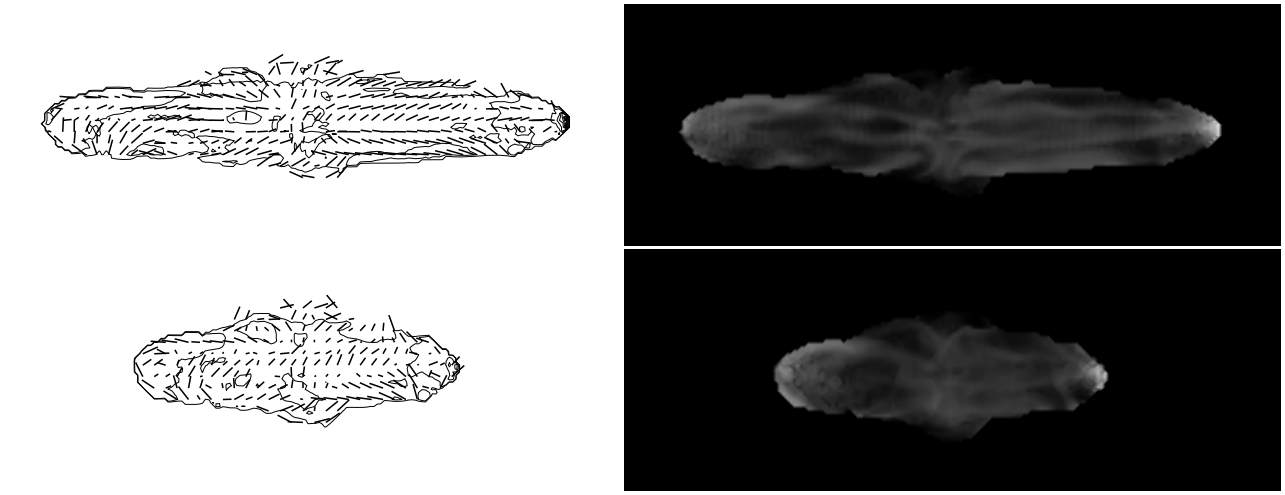

(b) Emission at $t_{jet} = 8.3$ Myr as a function of the viewing angle; $\theta_v = 60°$ (top) and $\theta_v = 30°$ (bottom).

Figure 7. Synthetic observations of the source with $\eta = 0.02$ and Mach = 40. Left: polarization maps. Vectors follow χ_B and their length is given by p. Vectors are superimposed on linear contours of $I/\langle I\rangle$. Right: logarithmic grey-scale maps of $I/\langle I\rangle$.

isotropic turbulence, in combination with the stretching of field lines in cocoons, predominantly along the jet direction.

The fractional polarization evolves quite differently. At the first time-step (Fig. 11, black profiles), we see that the p histograms are fairly similar and show a linear relation, rising monotonically towards larger p. As the cocoons with $\eta = 0.004$ grow, the profiles evolve into a peaked distribution with a broad peak between about $p = 0.2$ and 0.5. In contrast, the profiles for ($\eta = 0.02$, $\theta_v \geq 60°$) always peak at $p > 0.5$. The fractional polarization tells us about two things: (1) the degree of alignment of the field vectors that contribute to a given line of sight, and (2) the number of pixels along that line (assuming their contribution is different from each other). Hence we see the polarization generally decreasing for $\theta = 30°$. In cocoons where $\eta = 0.004$, we see a stronger p decline at

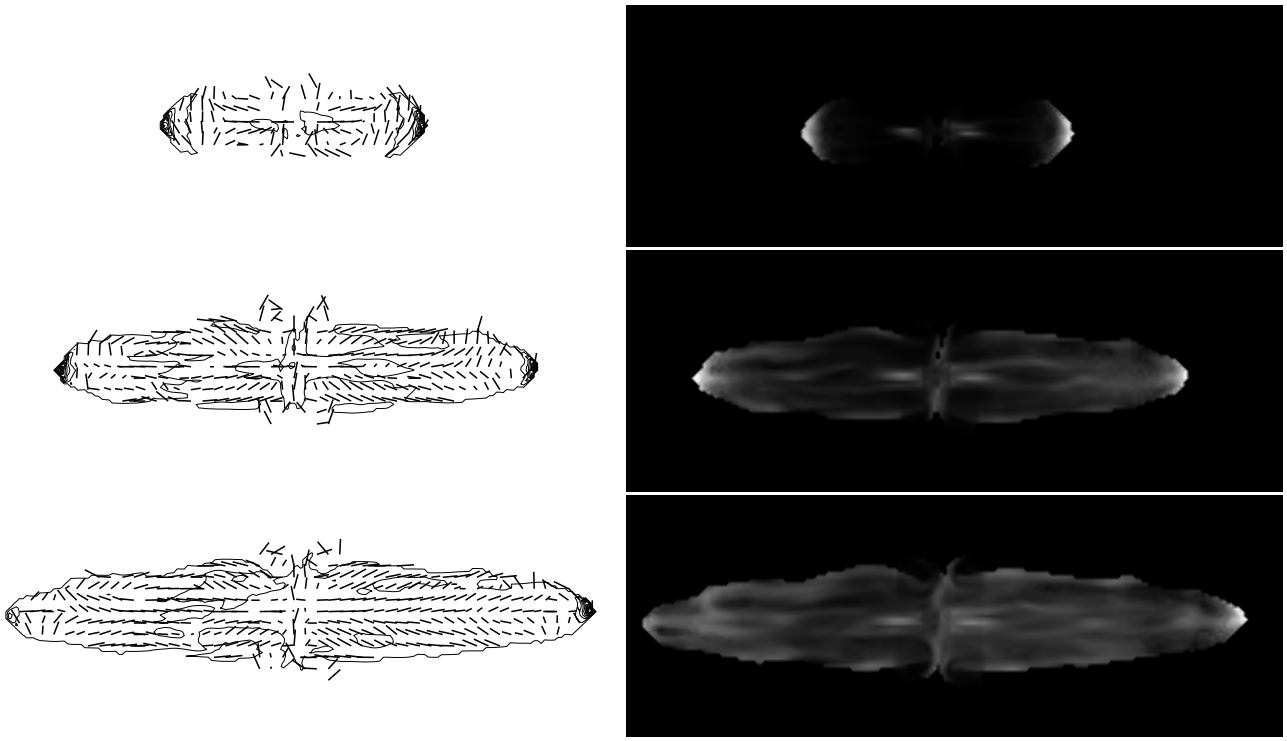

(a) Time evolution at $\theta_v = 90°$. From top to bottom $t_{jet} = \{1.8, 3.6, 4.4\}$ Myr.

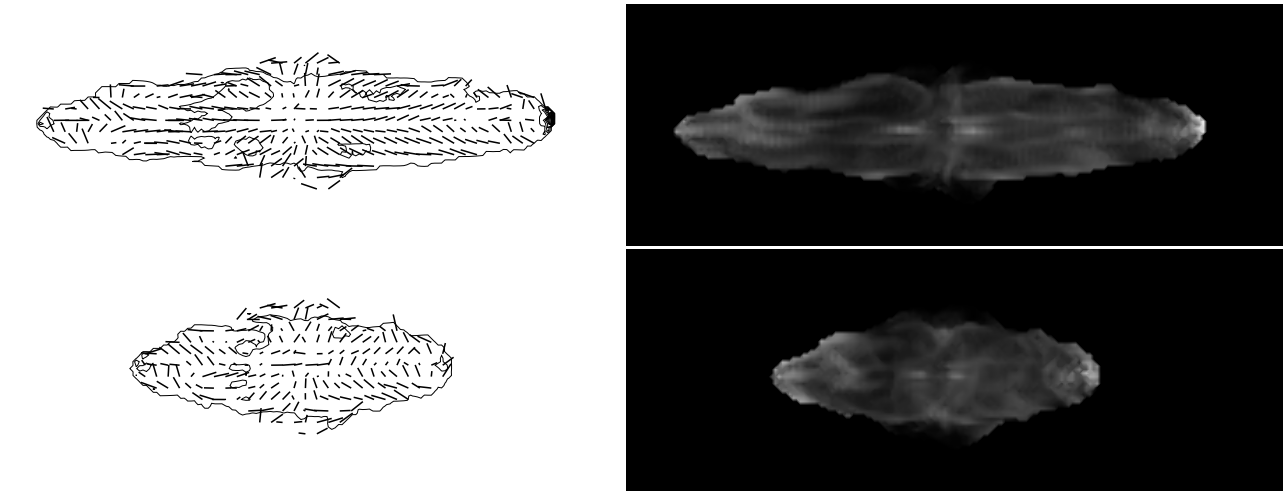

(b) Emission at $t_{jet} = 4.4$ Myr as a function of the viewing angle; $\theta_v = 60°$ (top) and $\theta_v = 30°$ (bottom).

Figure 8. Synthetic observations of the source with $\eta = 0.02$ and Mach = 80. Left: polarization maps. Vectors follow χ_B and their length is given by p. Vectors are superimposed on linear contours of $I/\langle I\rangle$. Right: logarithmic grey-scale maps of $I/\langle I\rangle$.

early times than later on. This occurs because their expansion slows down at late times, as these sources approach pressure equilibrium with the ambient medium. In cocoons where $\eta = 0.02$, on the other hand, we see a slow sideways growth and thus p drops very slowly. Moreover, we see higher polarization for larger η, again reflecting that high-density jets have more ordered magnetic fields and blow thinner cocoons.

We note that an additional set of synthetic polarization maps (not shown) was produced assuming a spatially uniform distribution of synchrotron emitting electrons [i.e. $p_c(\boldsymbol{x}, t) = 1$ in (12), for all $\boldsymbol{x}$ and t]. The polarimetric distribution of such maps was found to be very similar to the ones discussed in this section of the paper. Our results are not, therefore, sensitive to details of the electron distribution.

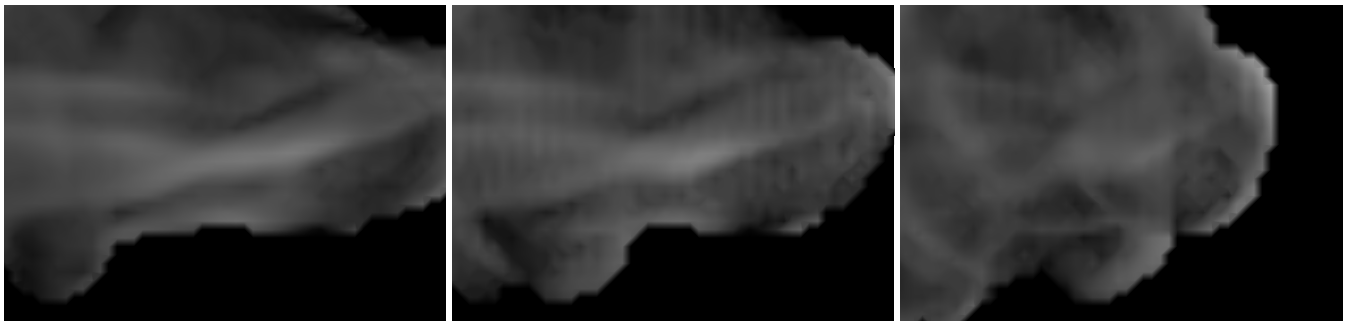

Figure 9. Synthetic emission filaments in the right lobe of the source with $\eta = 0.004$ and Mach = 40, at $t_{\rm jet} = 14.1$ Myr. The structure at the centre of the figures gets shorter and dimmer as the viewing angle decreases from 90° to 30°, from left to right, suggesting a tube-like geometry for the feature in question.

Radio source polarimetry is related with the study of cluster magnetic fields because they induce Faraday rotation and depolarization on the radio source emission (Pacholczyk 1963; Burn 1966). Faraday rotation maps contain information about the ICM's magnetic structure (for a review, see Carilli & Taylor 2002). In a sequel paper (Huarte-Espinosa, Krause, & Alexander, in preparation), we will investigate the evolution of cluster magnetic fields using statistical analysis on synthetic RM observations which are produced using the expanding model sources we present here.

4 DISCUSSION

About a handful of studies on synthetic synchrotron emission and polarimetry of extragalactic radio sources exist in the literature. We are not aware of any study that uses magnetic fields evolved in a MHD simulation self-consistently with the jet, as presented here.

Jones (1988) modelled relativistic jets with a turbulent magnetic field ansatz, advected with the flow velocity of the jet, to study the relation between linear and circular polarization in compact radio sources. The underlying hydrodynamic simulation is a conically expanding beam. With this ansatz, he gets a few, up to 23 per cent, linear fractional polarization. Though we start from a similarly turbulent field in our initial injection region, we get about 50 per cent linear fractional polarization in our beams. The reason is the order induced by the field line stretching described in more detail in Section 3.1. Models of jet collimation and acceleration typically require a poloidal field near the source (e.g. Porth & Fendt 2010, and references therein). The coherence length of this initial field should be small compared to observed jet sizes. Hence, stretching of the magnetic field in the beam seems to be an unavoidable consequence. The effect is also found by Gaibler et al. (2009). The latter study is however the only one we are aware of that has employed a zero gradient boundary condition in the jet nozzle.

Axisymmetric hydrodynamical simulations of collimated light jets, similar to our approach, were employed by Matthews & Scheuer (1990a) to simulate the advection and deformation of passive magnetic fields set up with an initial isotropic random geometry, similar to Jones (1988). Matthews & Scheuer implemented magnetic fields using passive tracer particles and followed the distortion of the fluid, at the respective position of tracer particles, by the velocity field computed in the hydrodynamic simulation. This gives a reasonable approximation of the magnetic field structure for dynamically passive magnetic fields. We also have a dynamically passive field, with a very similar initial, and slightly different nozzle boundary condition. In contrast to them, we do a full MHD treatment for the magnetic field. We confirm almost all of their results regarding the magnetic field structure: Matthews & Scheuer discuss in detail the toroidal and the poloidal stretching mechanism. As argued above, we believe the toroidal stretching mechanism is mainly responsible for the magnetic energy increase in cocoons. We do not observe a dominant toroidal field directly because non-axisymmetric shear converts this component to poloidal field. We generally see a predominantly axial field component in cocoons, consistent with their poloidal stretching mechanism. In contrast to them, we also find axially stretched and amplified magnetic fields in the beams.

As Matthews & Scheuer (1990a) do, we find field line stretching along the contact surface that separates cocoons from the ambient medium. In a resolution study, they show that the extent of that region gets smaller at higher resolution, but the field strength increases due to the increased shear. They also address synchrotron losses in the energy distribution of relativistic electrons. Due to such losses, they find that the aforementioned shear layer is very weak in synthetic radio maps. In our maps, these features appear as edge enhancements and are likely a numerical artefact because our treatment does follow synchrotron losses. In reality, the two fluids may slip easily and the shear layer may be insignificant. This depends on the magnetic viscosity of the plasma and is beyond the scope of this discussion.

Moreover, as we do, Matthews & Scheuer (1990a) find filaments in the synthetic emission images, but they report close to maximum fractional polarization. We find lower, more realistic, fractional polarization values in our simulations, especially for the lighter jets. The main reason for this difference is the breaking of axisymmetry. This allows for 3D turbulence in cocoons and for different directions of magnetic field vectors along the azimuthal direction. Yet, we also see fractional polarization values in the cocoon body, far away from the beams and the edges, which are still somewhat high. This might be a resolution issue: the magnetic field energy spectrum is close to Kolmogorov, which we have checked for the final snapshots of all our runs. Therefore, dominant structures are the large-scale ones, which we should be able to capture. However, the roughly 50 cells we have over the fatter cocoons might still be too little to capture some important small-scale structure that could reduce the fractional polarization. Our simulations show the fractional polarization is very similar for different jet velocities. Also, as Matthews & Scheuer (1990a) have already noted, cocoon magnetic fields are largely independent of the initial conditions prescribed at the base of the beams. It is therefore unlikely that there is something fundamental to the cocoon structure that we miss. Another reason for low fractional polarization might be that our jet densities may still be too high. We find the cocoon width, which is mainly regulated by the jet density, is an important factor for the polarimetry. Observed cocoons are usually wider relative to the beam than the ones we

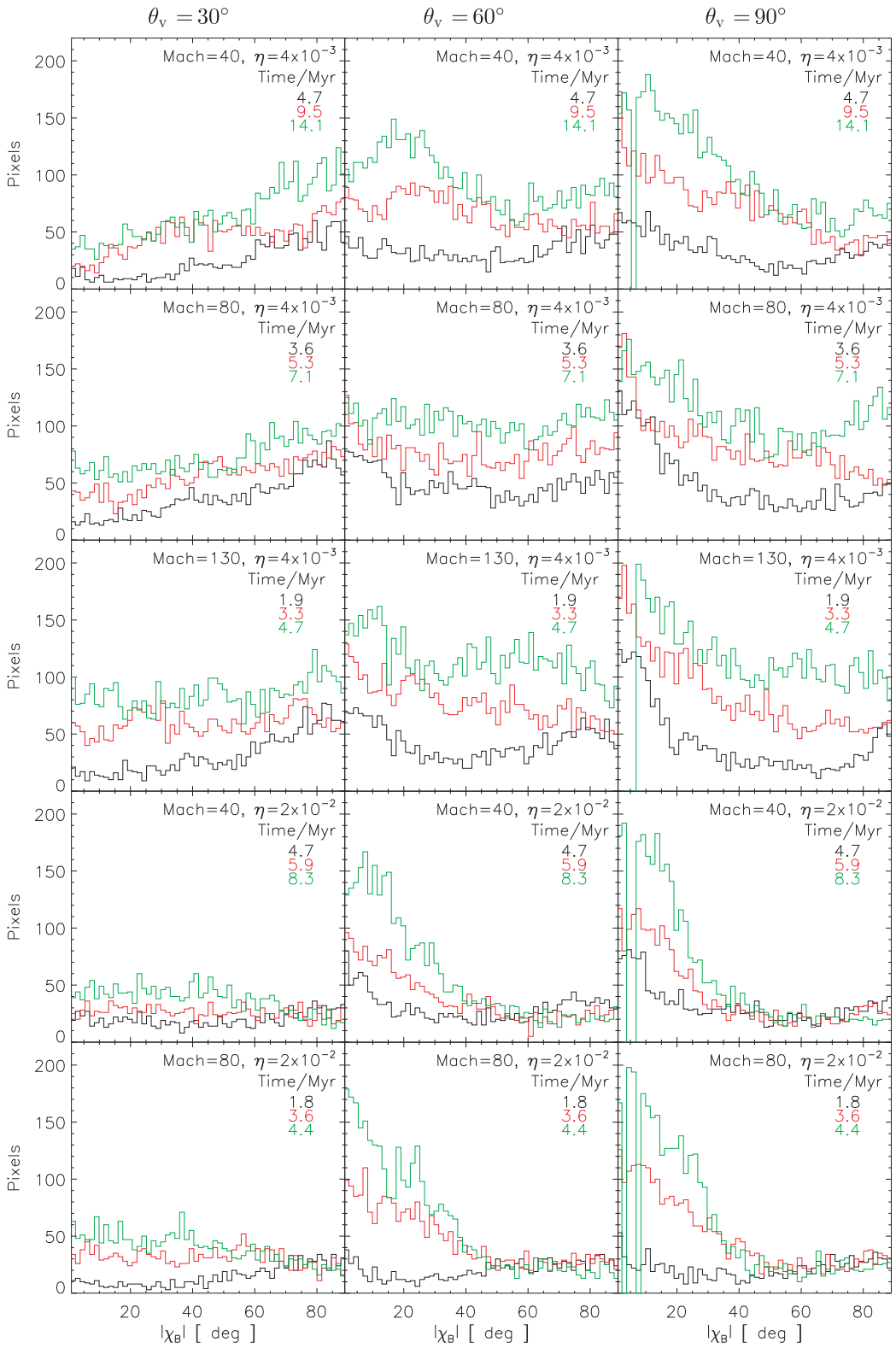

Figure 10. Histograms of $|\chi_B|$. θ_v increases from left to right, column-wise.

produce here. This fact indicates lower jet densities in the observed radio sources (Alexander & Pooley 1996; Krause 2003). Hence, low fractional polarization might be yet another consequence of jets being very light compared to their surroundings. Finally, Matthews & Scheuer (1990a) found small regions where field amplification and therefore synchrotron cooling became very significant in their simulations. In our 3D-MHD simulations, we see filaments in the cocoons (Figs 4–8, right column) and that magnetic fields there are about an order of magnitude stronger than the mean field. Thus we confirm the findings of Matthews & Scheuer (1990a).

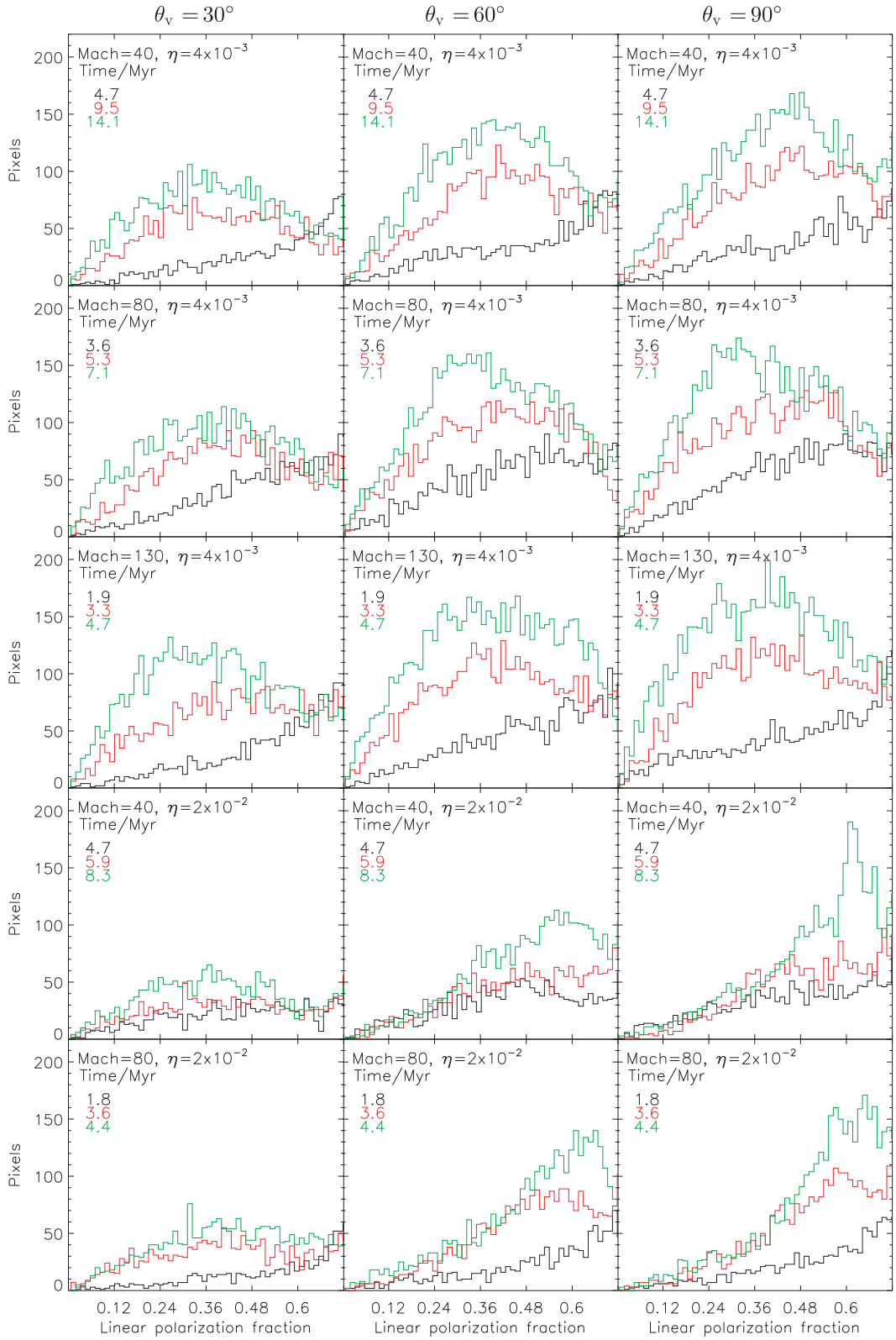

Figure 11. Histograms of the linear polarization degree. Panels are arranged as in Fig. 10.

Tregillis et al. (2001) carried out 3D-MHD simulations of a jet with $\eta = 0.01$, Mach $= 80$ and a helical magnetic field, the axial part of which extended throughout the computational domain. These authors studied the diffusive shock acceleration and transport of synchrotron relativistic electrons. We do not follow such processes. Then, Tregillis, Jones & Ryu (2004a) produced detailed synthetic observations of both the synchrotron and the X-ray – due Compton scatter from cosmic microwave background photons. They

emphasize that along the lines of sight that passes through strong shocks, most of the emission may come from regions close to the shock, and thus have close to maximum fractional polarization values. We might miss some of such regions due to the limitations of our simple model for the distribution of relativistic electrons. However, the emission from the bulk of cocoons cannot be dominated by such features, as the fractional polarization we predict for such regions is too high (compare above). This would mean that real radio lobes are relatively uniformly illuminated by relativistic electrons and are not dominated by relatively few isolated shock features.

5 SUMMARY AND CONCLUSIONS

We carried out 3D-MHD numerical simulations and synthetic observations to model magnetic fields in expanding FR II sources located at the core of a non-cool core galaxy cluster. A stratified fully ionized ICM was implemented, threaded by randomly tangled magnetic fields with a Kolmogorov power spectrum. Collimated, hypersonic and bipolar jets were injected in the centre of the computational domain. The geometry of the jets' magnetic fields is initially random, and then shaped by the dynamics of jets. Jets form cocoons filled with light gas and magnetic fields, the structure of which is determined by both the jets' backflow, via shear and compression, and the cocoon expansion.

We have presented five simulations exploring the parameter space given by jet-to-ambient density contrasts of $\eta = \{0.004, 0.02\}$, and jet velocities of $v_j = \{40, 80, 130\}$ Mach. We use the resulting model sources to produce synthetic synchrotron emission and linear polarization maps at viewing angles of $\theta_v = \{30^\circ, 60^\circ, 90^\circ\}$. The simulations have taught us the following.

While we do not inject magnetic energy at the jet nozzle, the magnetic energy in jets, and their host cocoons, increases with time. The amplification is stronger for wider cocoons, which are obtained for lighter and faster jets. The main amplification mechanism is the toroidal field line stretching (Matthews & Scheuer 1990b; Gaibler et al. 2009). The toroidal field is however quickly converted to poloidal field and the resulting field structure is hence a competition between MHD-turbulence and poloidal field stretching. Lighter jets are more turbulent and their magnetic field is therefore less aligned with the jet axis.

Our synthetic polarization maps are in good agreement with radio observations (e.g. Johnson et al. 1995; Gilbert et al. 2004; Mullin et al. 2006). We generally see B-vectors that are parallel to the jet axis, tangent to the source boundaries and perpendicular to strong emission gradients. The degree of linear polarization along both the jet axis and the source boundaries is higher than both inside and between radio lobes.

The cocoon magnetic structure shows a strong relation with η and a rather weak relation with v_j. In our polarization maps, this occurs because the projected sources' area on to the plane of the sky is proportional to the cocoons' volume. The intrinsic polarization angle distribution is consistently more uniform for $\eta = 0.02$ than in the lighter case. The mean polarization angle is $\sim 10^\circ$ smaller when $\eta = 0.02$ than in the lighter case. Also, the intrinsic linear polarization degree in the $\eta = 0.02$ case is higher than in lighter sources, i.e. when $\eta = 0.02$ we see p within 46–51 per cent in the cocoons and $\sim$63 per cent at the sources' edges. Conversely, when $\eta = 0.004$ we see p within 25–45 per cent in the cocoons and ~ 63 per cent at the edges. Even for our lighter cocoons, the fractional polarization is somewhat high away from the edges and beams, which might be a resolution issue or due to the fact that our cocoons are thinner than those of most observed FR II radio sources, which is related to the jet density.

The distribution of the polarization angle (magnetic vectors) depends on the viewing angle between jets and the line of sight, θ_v. On average, we see $\langle|\chi_B|\rangle$ decreases about 9° as θ_v goes from 30° to 60°, and about 4° as θ_v goes from 60° to 90°. In contrast, only $\langle p(\eta = 0.02)\rangle$ shows an increase of about 7 per cent as θ_v goes from 30° to 60°, and also about 3 per cent as θ_v goes from 60° to 90°. This is because cocoons have geometries similar to prolate spheroids, inside which the poloidal momentum flux is higher than the toroidal one. Cocoon magnetic fields are thus mainly stretched along the polar direction (the jet axis) which projection on to the line of sight is proportional to $\cos(\theta_v)$.

We see the main features of the $|\chi_B|$ histograms are shaped during the early expansion phase of sources, particularly for $\theta_v \gtrsim 60^\circ$. In this case, magnetic fields tend to align with the jet axis as sources grow. For $\theta_v = 30^\circ$, on the other hand, χ_B is distributed nearly isotropically. The fractional polarization is broadly distributed around about 30–40 per cent, and decreases in time.

ACKNOWLEDGMENTS

The software used in these investigations was in part developed by the DOE-supported ASC/Alliance Center for Astrophysical Thermonuclear Flashes at the University of Chicago. The authors wish to thank Dongwook Lee for the 3D-USM-MHD solver of FLASH3.1, and also to Malcolm Longair, Robert Laing, Julia Riley and Eric Blackman for useful discussions and comments that helped to improve this paper. MH-E acknowledges financial support from CONACyT (The Mexican National Council of Science and Technology, 196898/217314).

REFERENCES

Alexander P., Pooley G. G., 1996, in Carilli C. L., Harris D. E., eds, Cygnus A – Study of a Radio Galaxy. Cambridge Univ. Press, Cambridge, p. 149
Alexander P., Brown M. T., Scott P. F., 1984, MNRAS, 209, 851
Batten P., Clarke N., Lambert C., Causon D. M., 1997, SIAM J. Sci. Comput., 18, 1553
Begelman M. C., Cioffi D. F., 1989, ApJ, 345, L21
Black A. R. S., Baum S. A., Leahy J. P., Perley R. A., Riley J. M., Scheuer P. A. G., 1992, MNRAS, 256, 186
Blandford R. D., Rees M. J., 1974, MNRAS, 169, 395
Bridle A. H., Perley R. A., 1984, ARA&A, 22, 319
Burn B. J., 1966, MNRAS, 133, 67
Carilli C. L., Taylor G. B., 2002, ARA&A, 40, 319
Clarke D. A., 1993, in Röser H. J., Meisenheimer K., eds, Lecture Notes in Physics Vol. 421, Jets in Extragalactic Radio Sources. Springer, Berlin, p. 243
Clarke D. A., Norman M. L., Burns J. O., 1986, BAAS, 18, 909
Falle S. A. E. G., 1991, MNRAS, 250, 581
Fanaroff B. L., Riley J. M., 1974, MNRAS, 167, 31
Ferrari A., 1998, ARA&A, 36, 539
Frank A., Ryu D., Jones T. W., Noriega-Crespo A., 1998, ApJ, 494, L79
Fryxell B. et al., 2000, ApJS, 131, 273
Gaibler V., Krause M., Camenzind M., 2009, MNRAS, 400, 1785
Gilbert G. M., Riley J. M., Hardcastle M. J., Croston J. H., Pooley G. G., Alexander P., 2004, MNRAS, 351, 845
Guidetti D., Murgia M., Govoni F., Parma P., Gregorini L., de Ruiter H. R., Cameron R. A., Fanti R., 2008, A&A, 483, 699
Hardcastle M. J., Alexander P., Pooley G. G., Riley J. M., 1997, MNRAS, 288, 859

Hardcastle M. J., Alexander P., Pooley G. G., Riley J. M., 1998, MNRAS, 296, 4
Hardee P. E., Clarke D. A., Rosen A., 1997, ApJ, 485, 533
Heinz S., Reynolds C. S., Begelman M. C., 1998, ApJ, 501, 126
Högbom J. A., 1979, A&AS, 36, 173
Johnson R. A., Leahy J. P., Garrington S. T., 1995, MNRAS, 273, 877
Jones T. W., 1988, ApJ, 332, 678
Kaiser C. R., Alexander P., 1997, MNRAS, 286, 215
Keppens R., Meliani Z., van der Holst B., Casse F., 2008, A&A, 486, 663
King I. R., 1972, ApJ, 174, L123
Komissarov S. S., 1999, MNRAS, 308, 1069
Kössl D., Müller E., Hillebrandt W., 1990a, A&A, 229, 397
Kössl D., Müller E., Hillebrandt W., 1990b, A&A, 229, 401
Krause M., 2003, A&A, 398, 113
Krause M., Alexander P., 2007, MNRAS, 376, 465
Krause M., Camenzind M., 2001, A&A, 380, 789
Laing R. A., 1980, MNRAS, 193, 439
Laing R. A., 1981a, MNRAS, 195, 261
Laing R. A., 1981b, ApJ, 248, 87
Leahy J. P., Williams A. G., 1984, MNRAS, 210, 929
Leahy J. P., Pooley G. G., Riley J. M., 1986, MNRAS, 222, 753
Leahy J. P., Black A. R. S., Dennett-Thorpe J., Hardcastle M. J., Komissarov S., Perley R. A., Riley J. M., Scheuer P. A. G., 1997, MNRAS, 291, 20
Lee D., Deaane A. E., 2009, J. Comput. Phys., 228, 952
Leismann T., Antón L., Aloy M. A., Müller E., Martí J. M., Miralles J. A., Ibáñez J. M., 2005, A&A, 436, 503
Lind K. R., Payne D. G., Meier D. L., Blandford R. D., 1989, ApJ, 344, 89
Longair M. S., Ryle M., Scheuer P. A. G., 1973, MNRAS, 164, 243
Matthews A. P., Scheuer P. A. G., 1990a, MNRAS, 242, 616
Matthews A. P., Scheuer P. A. G., 1990b, MNRAS, 242, 623
Mignone A., Rossi P., Bodo G., Ferrari A., Massaglia S., 2010, MNRAS, 402, 7
Miller L., 1985, MNRAS, 215, 773
Mullin L. M., Hardcastle M. J., 2009, MNRAS, 398, 1989
Mullin L. M., Hardcastle M. J., Riley J. M., 2006, MNRAS, 372, 113
Murgia M., Govoni F., Feretti L., Giovannini G., Dallacasa D., Fanti R., Taylor G. B., Dolag K., 2004, A&A, 424, 429
Norman M. L., 1993, in Burgarella D., Livia M., O'Dea C. P., eds, Space Telescope Sci. Inst. Symp. Ser., Numerical Simulations of Astrophysical Jets. Cambridge Univ. Press, Cambridge, p. 211
Omma H., Binney J., Bryan G., Slyz A., 2004, MNRAS, 348, 1105
Pacholczyk A. G., 1963, Nat, 200, 765
Perley R. A., Dreher J. W., Cowan J. J., 1984, ApJ, 285, L35
Porth O., Fendt C., 2010, ApJ, 709, 1100
Press W. H., Teukolsky S. A., Vetterling W. T., Flannery B. P., 1992, Numerical Recipes in FORTRAN. Cambridge Univ. Press, Cambridge
Pudritz R. E., Ouyed R., Fendt C., Brandenburg A., 2006, in Reipurth B., Jewitt D., Keil K., eds, Protostars and Planets V. Univ. Arizona Press, Tucson
Rees M. J., 1971, Nat, 229, 312
Saikia D. J., Salter C. J., 1988, ARA&A, 26, 93
Scheuer P. A. G., 1974, MNRAS, 166, 513
Stone J. M., Hardee P. E., 2000, ApJ, 540, 192
Tregillis I. L., Jones T. W., Ryu D., 2001, ApJ, 557, 475
Tregillis I. L., Jones T. W., Ryu D., 2004a, ApJ, 601, 778
Tregillis I. L., Jones T. W., Ryu D., 2004b, J. Korean Astron. Soc., 37, 509
Tribble P. C., 1991a, MNRAS, 250, 726
Tribble P. C., 1991b, MNRAS, 253, 147
Vogt C., Enßlin T. A., 2003, A&A, 412, 373
Vogt C., Enßlin T. A., 2005, A&A, 434, 67

This paper has been typeset from a TEX/LATEX file prepared by the author.